

SUPER-RESOLUTION IMAGING AND CHARACTERIZATION

A Dissertation

Submitted to the Faculty

of

Purdue University

by

Dergan Lin

In Partial Fulfillment of the

Requirements for the Degree

of

Doctor of Philosophy

December 2019

Purdue University

West Lafayette, Indiana

THE PURDUE UNIVERSITY GRADUATE SCHOOL
STATEMENT OF DISSERTATION APPROVAL

Dr. Kevin J. Webb, Chair

Department of Electrical and Computer Engineering

Dr. Andrew M. Weiner

Department of Electrical and Computer Engineering

Dr. Dan Jiao

Department of Electrical and Computer Engineering

Dr. Mark R. Bell

Department of Electrical and Computer Engineering

Approved by:

Dr. Dimitrios Peroulis

Thesis Form Head

TABLE OF CONTENTS

	Page
LIST OF TABLES	v
LIST OF FIGURES	vi
ABSTRACT	xiii
1 INTRODUCTION	1
1.1 Super-Resolution Diffuse Optical Imaging	1
1.2 Temporal Scanning for Super-Resolution Diffuse Optical Imaging	2
1.3 Motion in Structured Illumination	3
2 SUPER RESOLUTION DIFFUSE OPTICAL IMAGING [†]	5
2.1 Diffuse Optical Imaging	5
2.2 Localization	9
2.2.1 Forward Model	10
2.2.2 Position Estimation	11
2.2.3 Multigrid for Super Resolution	13
2.3 Results	15
2.3.1 Simulation	16
2.3.2 Experiment	17
2.3.3 Resolution	24
2.4 Conclusion	24
3 LOCALIZATION WITH TEMPORAL SCANNING AND MULTIGRID FOR SUPER-RESOLUTION DIFFUSE OPTICAL IMAGING [†]	28
3.1 Models	28
3.1.1 Coupled Diffusion Equations	28
3.1.2 Forward Model for a Single Fluorescent Inhomogeneity	29
3.1.3 Forward Model for Multiple Fluorescent Inhomogeneities	32

	Page
3.1.4 Detector Noise	34
3.2 Localization for Super-Resolution Imaging	34
3.2.1 Localization of Multiple Fluorescent Inhomogeneities	34
3.2.2 Localization with Multigrid	38
3.3 Results	40
3.3.1 Localization for High Spatial Resolution	43
3.4 Discussion	45
3.5 Conclusion	46
4 MOTION IN STRUCTURED ILLUMINATION	47
4.1 Concept	47
4.2 Thin Film Characterization	51
4.3 Resolution	54
4.4 Detectability	54
4.5 Conclusion	58
5 FUTURE DIRECTIONS	59
5.1 Whole-Brain Fluorescent Imaging	59
5.2 Film Characterization and Defect Detection	60
REFERENCES	61
VITA	68

LIST OF TABLES

Table	Page
2.1 Estimated numerical and experimental localization uncertainties, means, and resulting resolution (mm). The resolution of FDOT is assumed to be depth/2.	25

LIST OF FIGURES

Figure	Page	
2.1	Resolution of diffuse optical imaging as reported in the literature. Red symbols are image reconstructions, where \blacktriangledown , \blacklozenge , \blacktriangleleft , \blacktriangle , \bullet , \blackstar , \blacktriangleright , and \blacksquare , correspond to [34–37, 45–48]. Blue symbols are solution measurements (no inversion was performed), \blacklozenge and where \blacksquare correspond to [32, 49]. The background μ'_s and μ_a used in each paper varies, but their average values are 0.85 mm^{-1} and 0.0063 mm^{-1} (close to those of tissue-simulating Intralipid), where μ'_s is between 0.5 and 1.0 mm^{-1} and μ_a is between 0 and 0.01 mm^{-1} . The blue curves are theoretical resolution limits for CW ($\omega = 0$) direct measurements, as calculated by Ripoll <i>et al.</i> [33]. The dashed blue curve was calculated using breast tissue parameters, where $\mu'_s = 1.5 \text{ mm}^{-1}$ and $\mu_a = 0.0035 \text{ mm}^{-1}$. The solid blue curve was calculated using the average values from the literature. The black curve is $\text{depth}/2$	8
2.2	Model geometry for an infinite slab of thickness d , where $\mathbf{r} = (x, y, z)$. An excitation source (X) at \mathbf{r}_s and a fluorescence emission detector (O) at \mathbf{r}_i are placed one scattering length $l^* = 3D$ away from the slab boundaries as shown. A fluorescence source (\bullet) is at the unknown position \mathbf{r}_f . Zero flux ($\phi = 0$) boundary conditions with $l_s = 5.03D$ are used to simulate an infinite slab geometry [21].	12

- 2.3 Slab problem geometry and a demonstration of the localization of a point fluorescent source with high discretization error. (a) Slab problem geometry with $\mathbf{r}_s = (8.09, 9.07, 1.11)$ mm plotted as the red point, $\mathbf{r}_{ft} = (12.77, 10.79, 5.0)$ mm plotted as the green point, and $N = 400$ detector locations \mathbf{r}_i plotted as blue points. The slab is 18 mm thick with $\mu'_s = 0.9 \text{ mm}^{-1}$ and $\mu_a = 0 \text{ mm}^{-1}$. These positions were used so that the simulation and experimental results can be compared. The slab has the same dimensions and properties as used in the experiment. Measurements were simulated using (2.4) with $w = 10$ and a 30 dB SNR, and $\tilde{w}(\mathbf{r}_f)$ from (2.7) and $c(\mathbf{r}_f)$ from (2.8) were evaluated over the region of interest. (b) Plot of $\tilde{w}(\mathbf{r}_f)$ slice and (c) plot of $c(\mathbf{r}_f)$ slice for fixed y , such that the plots contains the point that minimizes $c(\mathbf{r}_f)$. Here, $y = 10.59$, and the color bars have log scales with arbitrary units. Using (2.9), $\hat{\mathbf{r}}_f = (12.94, 10.59, 5.29)$, and using (2.10), $\hat{w} = 10.07$. The localization errors in the x , y , and z dimensions are 1.37%, 1.85%, and 5.88%, respectively. The course discretization of the region of interest is a primary contributor to the estimation error. (d) Localization with multiresolution. Plots of $c(\mathbf{r}_f)$ slices for fixed y are shown for multiresolution iterations 1, 2, 3, and 13. At iteration 13, from (2.9), $\hat{\mathbf{r}}_f = (12.77, 10.78, 4.98)$, and from (2.10), $\hat{w} = 10.02$. The localization errors in the x , y , and z dimensions are 0.05%, 0.05%, and 0.19%, respectively. The discretization error has been minimized. 14
- 2.4 Uncertainty in the numerical localization of a fluorescent inhomogeneity in the slab geometry shown in Fig. 2.3(a). The standard deviations were estimated using 50 noisy independent measurements that were generated using (2.11). (a) $\hat{\sigma}_x$, $\hat{\sigma}_y$, and $\hat{\sigma}_z$ versus SNR plotted as red, green, and blue curves, respectively. The depth of the fluorescent inhomogeneity was 13 mm, as shown in Fig. 2.3(a). $\hat{\sigma}_z$ is larger than $\hat{\sigma}_x$ and $\hat{\sigma}_y$ because the detectors are only in the $x - y$ plane. (b) Ellipses in the $x - y$ plane with major and minor axes of lengths $4\hat{\sigma}_x$ or $4\hat{\sigma}_y$ and means given by their center point. Red, green, and blue ellipses correspond to SNRs of 15 dB, 25 dB, and 40 dB, respectively. (c) $\hat{\sigma}_x$, $\hat{\sigma}_y$, and $\hat{\sigma}_z$ versus depth plotted as red, green, and blue curves, respectively, with 30 dB SNR. (d) Ellipses in the $x - y$ plane with major and minor axes of length $4\hat{\sigma}_x$ or $4\hat{\sigma}_y$ and means given by their center point. Red, green, and blue ellipses correspond to depths of 13 mm, 8 mm, and 5 mm, respectively. 18

Figure	Page
2.5 (a) Experiment setup for localization of a fluorescent inhomogeneity (green point). The fluorescent inhomogeneity (ATTO 647N) is embedded in a highly scattering slab that is 18 mm thick. The laser source is a filtered pulsed supercontinuum source (EXR-20 NKT Photonics, 5 ps seed pulse width, 20 MHz repetition rate, VARIA tunable filter). The laser source is tuned to λ_x , and detection is by a CCD camera with or without a bandpass filter at λ_m . (b) Light at λ_x detected by the CCD camera without the bandpass filter. Because the bandpass filter attenuates the excitation light by a factor of 10^6 , the fluorescent signal is negligible compared to the transmitted excitation light when the bandpass filter is not used. (c) Light at λ_m (after background subtraction) detected by the CCD camera with the bandpass filter. The positions of the 400 detectors are shown as blue dots. (d) CCD image of a ruler showing the field of view (about 22.02 mm by 22.02 mm). Images of the ruler were used to convert pixels to mm.	22
2.6 Experimental localization uncertainty for the fluorescent inhomogeneity embedded in the highly scattering slab of Fig. 2.5. Experimental values for $\hat{\sigma}_x$, $\hat{\sigma}_y$, and $\hat{\sigma}_z$ were estimated using 50 independent experimental measurements. (a) Plot of the (x, y) components of the localized positions as blue points. These points were used to calculate the major and minor axes of the red ellipse, which have dimensions $4\hat{\sigma}_x$ or $4\hat{\sigma}_y$, as well as its center red point, which is the mean. The black point is the true location that was estimated with a 2-D Gaussian fit. (b) Comparison of the experimental uncertainty to the numerical uncertainty. The blue ellipse was generated from numerical data with mean SNR= 28.9 dB to match the experimental value, and the red ellipse is the same as in (a). See Table 2.1 for the numerical values.	23
3.1 Model geometry with position vector $\mathbf{r} = (x, z)$. Excitation sources at λ_x (red) are placed at known positions \mathbf{r}_s , point fluorescence emission locations are assumed to be \mathbf{r}_f (green), and detectors at λ_m are placed at known positions \mathbf{r}_d (blue).	31

Figure	Page	
3.2	Typical fluorescence temporal responses for one source and seven detectors ($Q = 1, M = 7$). The optical properties are similar to tissue, where $\mu'_s = 2 \text{ mm}^{-1}$, $\mu_a = 0.02 \text{ mm}^{-1}$, and $n = 1.33$, giving a mean free path length $l^* = 3D = 0.5 \text{ mm}$. The 7 different symbols and corresponding colors represent different source-detector measurement pairs. The time axis is a discrete set of points t_1, \dots, t_N , with T between sample points. (a) The delay τ_2 is short, causing substantial overlap due to superposition. (b) The delay τ_2 is long such that the detected fluorescence decays substantially before the next fluorescence response. We show that localization of the fluorescence inhomogeneities is possible in both cases.	36
3.3	Localization of a single fluorescent inhomogeneity ($K = 1$) using an (x, z) coordinate system. 1 source (green) and 7 detectors (red) are placed at the boundary of a square of side length $32l^*$. The optical properties are the same as in Fig. 3.2, where $l^* = 0.5 \text{ mm}$, and we assume an SNR of 30 dB. A fluorescent inhomogeneity with $\eta_1 = 0.1 \text{ mm}^{-1}$ was placed at $x = 15.26 \times l^*$ and $z = 15.56 \times l^*$. The simulated noisy data is the same as the first set of curves at τ_1 shown in Fig. 3.2(b). (a) Yield $\tilde{\eta}_k(\mathbf{r}_{f_k})$ from (3.20) plotted over the region of interest. (b) Cost $c_k(\mathbf{r}_{f_k}, \tau_k)$ from (3.21) plotted over the region of interest. The position with lowest cost in (b) is $\hat{\mathbf{r}}_{f_k}$, and the value of $\tilde{\eta}_k$ at $\hat{\mathbf{r}}_{f_k}$ in (a) is $\hat{\eta}_k$. Here, $\hat{\mathbf{r}}_{f_k} = (x, z) = (15.24, 15.75) \times l^*$ and $\hat{\eta}_k = 0.0999 \text{ mm}^{-1}$. The percent errors in the estimated x and z positions are 0.143% and 1.196%, respectively. The discretization of the region of interest is a primary contributor to the estimation error.	39
3.4	Localization with MRA of the single fluorescent inhomogeneity in Fig. 3.3. The cost is calculated using (3.20) and (3.21) on progressively finer grids, where each new grid contains the region of smallest cost. Here, $\hat{\mathbf{r}}_{f_k} = (x, z) = (15.27, 15.57) \times l^*$ and $\hat{\eta}_k = 0.1003 \text{ mm}^{-1}$. The percent errors in the estimated x and z positions are 0.037% and 0.066%, respectively. The discretization error has been reduced, especially for the z coordinate. The number of positions where the cost must be calculated has also been reduced, decreasing the computation time. The reduction is even greater when extrapolated to 3D.	41

- 3.5 Localization of four fluorescent inhomogeneities at different positions with different delays and yields using the same optical parameters as in Fig. 3.2 and the same geometry as in Fig. 3.3. The true parameters describing the inhomogeneities are $(x, z, \eta, \tau) = (15l^*, 15l^*, 0.1, 5T), (15l^*, 15.2l^*, 0.15, 20T), (15.2l^*, 15.0l^*, 0.075, 40T),$ and $(15.2l^*, 15.2l^*, 0.05, 46T),$ where $l^* = 0.5$ mm and $T = 0.19$ ns. All of these parameters are estimated by the algorithm. We assume the fluorescence lifetime τ_f is known. (a) Problem geometry as in Fig. 3.3, where the positions of the excitation source (green), detectors (red), and fluorescent inhomogeneities (cyan) are plotted. (b) Detected fluorescence temporal profile. One source ($Q = 1$) and seven detectors ($M = 7$) give 7 measurements \mathbf{y}_{qm} . The 7 different symbols and their corresponding colors represent different source-detector measurement pairs. The data was generated using the true parameters with 30dB of simulated noise. (c) True positions of the inhomogeneities \mathbf{r}_k and the estimated positions $\hat{\mathbf{r}}_{f_k}$ determined by the localization algorithm. Note the accuracy of the estimated positions. (d) Yield η_k experimental errors. Labels one to four correspond to delays from shortest to longest. Each fluorescent inhomogeneity was successfully localized, even for the case when there is overlap between the temporal signals. 42
- 3.6 Localization uncertainty of a single fluorescent inhomogeneity using the same optical parameters as in Fig. 3.2 and the same geometry as in Fig. 3.3 with $Q = 1$. The fluorescent inhomogeneity location was estimated 150 times using noisy simulated independent data sets. The true location is the black point. The ellipses have major and minor axes of length $4\sigma_x$ or $4\sigma_z$, such that they contain 95% of the \hat{x} and \hat{z} positions. The center points of the ellipses are the mean of the \hat{x} and \hat{z} positions. (a) Localization uncertainty for different SNR with $M = 7$ and $w = 3T$. Blue, green, and red correspond to SNR of 30, 20, and 10 dB, respectively. (b) Zoomed version of (a) to show the mean values. (c) Localization uncertainty for different numbers of detectors M with 30 dB noise and $w = 3T$. Red, green, and blue correspond to $M = 7, M = 31,$ and $M = 50$. (d) Enlarged version of (c) to show the mean values. (e) Localization uncertainty for different window lengths w , 30 dB SNR, and $M = 7$. Red, green, and blue correspond to windows $w = 32T, 17T,$ and $2T,$ where $T = 0.19$ ns and $t_{max} = 64T$. (f) Enlarged version of (e) to show the mean values. The ellipses are not circles because the fluorescent inhomogeneity is not located at the center of the medium and equidistant to all detectors. Note that the fluorescent inhomogeneity can be accurately localized even with low SNR, few detectors, and a short window w 44

Figure	Page	
4.1	The simulated measurement arrangement has a plane wave incident from the top, with the free-space wavelength as $\lambda = 1.5\mu\text{m}$. Two dielectric slabs act as partially reflecting mirrors and form a low- Q cavity with a length of 2.7λ (inner face-to-face distance). An object comprised of a thin film on top of a substrate, and a total thickness of $T = \lambda/5$, is located in this cavity and moved vertically upwards in nm-scale increments. As the object is translated in the cavity to a set of positions, the power is measured at the detector plane, located 0.4λ below the bottom surface of the lower mirror.	49
4.2	Measured power flow against object position for different film parameters. The end-to-end length of the error bars is equal to 4σ , calculated with an SNR of 30 dB. (a) Film with $L = 0.005\lambda$ and varying refractive indices, n . (b) Film with $n = 2.00$ and different thicknesses, L . (c) Expanding the scale in (a), the red curve uses $S(\Delta y; L, 1.95)$ as a reference by setting it to zero, and the blue curve gives $[S(\Delta y; L, 2.00) - S(\Delta y; L, 1.95)]$. (d) Expanding the scale in (b), the red curve shows $S(\Delta y; 0.005\lambda, n)$ as a reference (zero), and the blue curve $[S(\Delta y; 0.007\lambda, n) - S(\Delta y; 0.005\lambda, n)]$	50
4.3	Calculated costs for a thin film substrate by comparing the simulated noisy experimental measurements with forward calculations of different film configurations without multiresolution (top left), and with multiresolution (starting from top right and following the arrows). The film substrate used in the simulated experiment has a film thickness $L_t = 0.006\lambda$ and refractive index $n_t = 1.72$. Without multiresolution, forward calculations were made for different combinations of film thicknesses $L \in [0.002\lambda, 0.022\lambda]$ with step increments of 0.002λ , and refractive indices $n \in [1.62, 1.98]$ with step increments of 0.04, resulting in an 11x11 grid. The cost is minimized at the correct parameters where $\hat{L} = 0.006\lambda$ and $\hat{n} = 1.72$. When using a multiresolution approach, forward calculations were made on a coarse 5x5 grid with a significantly increased range of values of $L \in [0.002\lambda, 0.13\lambda]$ and $n \in [1, 3.56]$. The cost is calculated iteratively on zoomed in regions of interest (following the arrows) that encompasses the the point of minimum cost.	53

Figure	Page	
4.4	500 independent measurements were made at different SNR values to calculate a distribution of reconstructed values of $L/1000\lambda$ and n , representing uncertainty in the reconstruction of thin film parameters. (a) Box plots of the distribution of reconstructed film thicknesses for different SNR values. Note that the y -axis is on the scale of 10^{-3} . (b) Box plots of the distribution of reconstructed refractive indices. The top edge of the box represent the upper quartile of the reconstructed values, and the bottom edge represent the lower quartile. The whiskers extend to the upper and lower extremes, and the red dots represent outliers. In both plots, the median (red dashed line) obtained from the set of reconstructed values is equal to the the true film thickness and refractive index, L_t and n_t	55
4.5	Minimum detectability of very thin films with low index contrast relative to the optical properties of the slab. The region to the right and above of each curves represent detectability above 99.99% for when a thin film is present from noisy measurement data. (a) The dashed black, solid red, and dashed-dotted blue curves correspond to 35 dB, 30 dB, and 25 dB, respectively. (b) At a SNR = 30 dB, the solid red, dashed black, and dashed-dotted blue curves correspond to when the number of positions, K , equals 21, 11, 5, respectively.	57

ABSTRACT

Lin, Dergan , Purdue University, December 2019. Super-Resolution Imaging and Characterization. Major Professor: Kevin J. Webb.

Light in heavily scattering media such as tissue can be modeled with a diffusion equation. A diffusion equation forward model in a computational imaging framework can be used to form images of deep tissue, an approach called diffuse optical tomography, which is important for biomedical studies. However, severe attenuation of high-spatial-frequency information occurs as light propagates through scattering media, and this limits image resolution. Here, we introduce a super-resolution approach based on a point emitter localization method that enables an improvement in spatial resolution of over two orders of magnitude. We demonstrate this experimentally by localizing a small fluorescent inhomogeneity in a highly scattering slab and characterize the localization uncertainty. The approach allows imaging in deep tissue with a spatial resolution of tens of microns, enabling cells to be resolved.

We also propose a localization-based method that relies on separation in time of the temporal responses of fluorescent signals, as would occur with biological reporters. By localizing each emitter individually, a high-resolution spatial image can be achieved. We develop a statistical detection method for localization based on temporal switching and characterization of multiple fluorescent emitters in a tissue-like domain. By scaling the spatial dimensions of the problem, the scope of applications is widened beyond tissue imaging to other scattering domains.

Finally, we demonstrate that motion of an object in structured illumination and intensity-based measurements provide sensitivity to material and subwavelength-scale-dimension information. The approach is illustrated as retrieving unknown parameters

of interest, such as the refractive index and thickness of a film on a substrate, by utilizing measured power data as a function of object position.

1. INTRODUCTION

1.1 Super-Resolution Diffuse Optical Imaging

The interaction of light with tissue has received intense study due to a myriad of applications in biomedical science [1–4]. Near the tissue surface, coherent methods enable imaging with a spatial resolution at the diffraction limit [5–7]. However, in deep tissue, where the propagation direction of light is randomized due to optical scattering, forming an image becomes a much greater challenge.

Deep-tissue imaging is achievable with diffuse optical imaging (DOI), a computational imaging method where a model of light transport in scattering media allows extraction of images from incoherent intensity measurements [2, 8–10]. For example, in diffuse optical tomography (DOT), three-dimensional images of the spatially dependent optical properties are iteratively reconstructed from boundary measurements of highly scattered light [10–13]. With the addition of fluorescent contrast agents, fluorescence diffuse optical tomography (FDOT) allows computational imaging of targeted biochemical pathways [14, 15]. FDOT has proven especially useful for *in vivo* small animal studies of, for example, targeted drugs [16] and protein misfolding [17]. However, the low resolution of DOI methods such as FDOT compared to coherent methods [18], which are typically near-surface (≤ 1 mm), has restricted the applications.

In Chapter 2, we present a method to circumvent previous DOI resolution limits. We use optical localization, where information about the location of the centroid of an inhomogeneity is extracted. We call the method super-resolution diffuse optical imaging (SRDOI). The case we consider is a small region embedded in a heavily scattering background that contains fluorophores. Multiple fluorescent regions could be similarly imaged at high resolution when the emission from each region is sepa-

rable, for example, through sufficient spatial, temporal, or spectral separation, or a combination of these. The results indicate that by localizing many inhomogeneities individually within a highly scattering medium and combining the positions into a single image, high-resolution DOI can be achieved. Previous studies have localized fluorescent inhomogeneities in deep tissue [19–22]. For example, boundary measurements of fluorescence emission have allowed extraction of the location of fluorescing tumors [21, 23]. In these studies, tumor masses were localized after injecting mice with fluorescent contrast agents that targeted specific cancer cells. However, the implications and limits for high resolution imaging have not been previously examined.

1.2 Temporal Scanning for Super-Resolution Diffuse Optical Imaging

Super-resolution methods have been developed for improving the spatial resolution beyond the diffraction limit in microscopy. Fundamentally, imaging methods can surpass resolution limits with the addition of prior information to compensate for the information that is lost due to attenuation or randomization of the signal. For example, structured illumination microscopy (SIM) [24] breaks the resolution limit through spatial modulation of coherent light sources. Stimulated emission depletion (STED) [25] forms a smaller effective point spread function (PSF) by saturating fluorophores at the periphery of the focal point. Other techniques, such as photoactivated localization microscopy (PALM) [26] and stochastic optical reconstruction microscopy (STORM) [27], are able to localize switchable fluorescent molecules by distinguishing the emission between their fluorescent and non-fluorescent states. A method to achieve super-resolution imaging in a heavily scattering medium would be important for deep-tissue *in vivo* imaging.

Fluorescence imaging has become a standard tool in biomedical research because modulation of fluorescence intensity in space and time can provide information on biochemical processes [28–30]. Methods such as confocal microscopy [31] have enabled high-resolution fluorescence imaging near the surface of tissue. However, imaging in

deep tissue, where the propagation direction of light becomes randomized, presents a major challenge in optical imaging. Information is lost due to scatter and absorption, which hinders image formation. Diffuse optical imaging methods have been developed to overcome the detrimental effects of scatter, enabling deep tissue fluorescence imaging [28]. The dependence of the spatial resolution on depth is nonlinear, but for typical tissues, measurement geometries, and beyond a depth of about 1 cm, spatial resolutions of about depth/2 have been achieved [32–38].

In Chapter 3, we present a localization-based method that allows for super-resolution diffusive optical imaging in highly scattering media, such as tissue. The method relies on some degree of separation in time of the temporal response of multiple fluorescent sources. By localizing each emitter individually, a spatial resolution on the order of 10 microns through 1 cm of tissue or more is possible.

1.3 Motion in Structured Illumination

The broad need for determining the optical properties of thin films in a multitude of applications is generally served by ellipsometry [39]. Ellipsometry measures the amplitude ratio and the phase difference between polarized light reflected from the surface of a film and determines parameters such as the refractive index and thickness by fitting the experimental data to an optical model that represents an approximated sample structure [39]. Generally, a model of the frequency-dependent dielectric constant is used for successful parameter extraction. For example, such a model may represent a Lorentzian resonance or impose a Drude model. While simplifying the extraction, this imposes a description that is both approximate and not necessarily correct .

In Chapter 4, we demonstrate motion in structured illumination as a means to obtain additional measurement data and hence avoid the need for a material response model. The structured field is obtained using a cavity. There is a long history of using interferometers to determine the relative position of a surface, and white-light

interferometry has been used to retrieve the thickness of thin films [40], under the assumption that the frequency-dependent dielectric constant is known. We present an interferometer arrangement where measurements as a function of the controlled position of the sample, as could be achieved with a piezoelectric positioner, allows the extraction of both the thickness and the dielectric constant based on transmission measurements. The simple intensity-based measurement required avoids the alignment and multiple polarization data typical of ellipsometry. Here, the film is moved in a structured background field in steps, and the total power due to the background and scattered fields is measured. The method relies on cost-function minimization using a forward model to compare the measurements to a set of forward model data corresponding to different sample structures, rather than repeated corrections to a theoretical dielectric function and initial values in order to fit the experimental data. Imaging methods based on object motion in structured illumination have been proposed for achieving far-subwavelength resolution using far-field measurements [41]. The film characterization approach described here is a 1D implementation where it is shown that both the dimension and the dielectric constant of a film can be determined using a forward model. Also, measured intensity correlations over object position with motion in a speckled field have shown that both macroscopic and microscopic information is available [42], although in this case extraction is through statistical averaging using intensity data, yielding normalized geometric information about the object, and a forward model is not plausible.

2. SUPER RESOLUTION DIFFUSE OPTICAL IMAGING[†]

We consider the general case of localizing small fluorescent inhomogeneities in three-dimensional (3D) space that are embedded within scattering media. We call the method super-resolution diffuse optical imaging (SRDOI). In Section 2.1, we describe light propagation in highly scattering media and examine the spatial resolution in deep tissue that has been achieved by diffuse optical imaging (DOI) as a comparison for SRDOI. In Section 2.2, the fluorescent localization method is described, including the derivation of the forward model and the optimization procedure. In Section 2.3, we characterize the performance of SRDOI with numerical simulation and experimental validation in a slab geometry. Our results demonstrate two orders of magnitude improvement in the spatial resolution compared to fluorescence diffuse optical tomography (FDOT).

2.1 Diffuse Optical Imaging

Optical transport in tissue can be described by the radiative transfer equation, and under restrictions on scattering strength (weak), absorption (weak), and time (long compared to the scattering time), and with sufficient scatter, the diffusion approximation provides a simple model [10, 11]. In the frequency domain, the light source is modulated at angular frequency ω , i.e., we assume $\exp(-i\omega t)$ variation.

[†] This work is published as B. Z. Bentz, D. Lin, K. J. Webb, “Superresolution Diffuse Optical Imaging by Localization of Fluorescence,” *Phys. Rev. Appl.*, vol. 10, no. 3, p. 034021, 2018 (Ref. [43])

For a fluorescence source in a locally homogeneous medium, the coupled diffusion equations can then be written in the form of wave equations as [15]

$$\nabla^2 \phi_x(\mathbf{r}) + k_x^2 \phi_x(\mathbf{r}) = -S_x(\mathbf{r}, \omega) \quad (2.1)$$

$$\nabla^2 \phi_m(\mathbf{r}) + k_m^2 \phi_m(\mathbf{r}) = -\phi_x(\mathbf{r}) S_f(\mathbf{r}, \omega), \quad (2.2)$$

where \mathbf{r} denotes position, ϕ (W/mm²) is the photon flux density, the subscripts x and m , respectively, denote parameters at the fluorophore excitation and emission wavelengths, λ_x and λ_m , $k^2 = -\mu_a/D + i\omega/(Dv)$, where $D = 1/[3(\mu'_s + \mu_a)]$ (mm) is the diffusion coefficient, μ'_s is the reduced scattering coefficient, μ_a is the absorption coefficient, v is the speed of light within the medium, $S_x(\mathbf{r}, \omega)$ is the excitation source, and $S_f(\mathbf{r}, \omega)$ describes the fluorescence emission. In an infinite homogeneous space, the frequency domain diffusion equation (written as a lossy wave equation) Green's function is

$$g(\mathbf{r}', \mathbf{r}) = \frac{e^{ik|\mathbf{r}-\mathbf{r}'|}}{4\pi|\mathbf{r}-\mathbf{r}'|}, \quad (2.3)$$

where \mathbf{r}' is the position of a point source and the complex wave number k is applied at λ_x or λ_m in (2.1) or (2.2) respectively.

Solutions to (2.1) and (2.2) are called diffuse photon density waves (DPDW's) [2, 33, 44]. Here, we refer to data formed through experimental detection of DPDW's as measurements. In contrast, images recovered using an inversion method (an indirect imaging method that extracts desired parameters (e.g., \mathbf{r}') from measurement data (e.g., ϕ) through inversion of a forward model) are referred to as reconstructed images. The resolution of a reconstructed image depends on the method used (see for example, [34, 36]). Of note, the treatment of the nonlinear nature of the inversion process and the use of constraints can be of substantial consequence.

Even without absorption, the DPDW wavenumber is complex, implying that there is always both propagation and attenuation at any spatial frequency [33]. The wavelength of DPDW's for typical tissue and modulation frequencies (10 MHz or so) is on the order of a few centimeters. Measurements are therefore usually made within distances less than about one wavelength from a source location, placing them in

the near field in this sense. However, the attenuation of high spatial frequencies is still severe, causing a significant reduction in resolution with depth. Here, we define resolution as the full width at half max (FWHM) of the point spread function (PSF), where the PSF is the image of a point source located in the scattering medium. Equivalently, the resolution is the distance between two identical point sources such that their PSFs intersect at their FWHM.

The dependence of the resolution on depth is nonlinear and has been estimated using the FWHM of the propagation transfer function in a homogeneous infinite medium [33]. The resolution is unrelated to the diffraction limit because DPDW's have a complex wavenumber and are measured in the near field. The resolution depends primarily on μ'_s , μ_a , and the distance from the source to detectors. Practically, however, the resolution depends on many other factors, including the measurement signal-to-noise ratio (SNR), the medium geometry, the source-detector diversity, the contrast between the inhomogeneity and the background, and the experimental setup. For the case of reconstructed images, the resolution will also depend on the computational method used for reconstruction.

As a comparison for the work presented here, Fig. 2.1 shows a plot of the resolutions achieved based on both measured data (without reconstruction of an image) and image reconstructions (though a computational imaging procedure). The red symbols are reconstructed image resolutions (without prior information), and the blue symbols are direct measurement resolutions. The blue curves are analytical resolution limits of direct measurements for μ'_s and μ_a typical of tissue, as calculated by Ripoll *et al.* [33]. From Fig. 2.1, we find that for optical properties similar to tissue and beyond a depth of about 1 cm, the reported reconstructed image resolution is typically about depth/2, as represented by the dashed black line.

The resolution in Fig. 2.1 can be improved with the incorporation of prior information that constrains the inverse problem. When combined with other imaging modalities, such as MRI [50, 51], the resolution can be improved to that of the higher resolution method. Here, we show that the resolution of DOI can be greatly im-

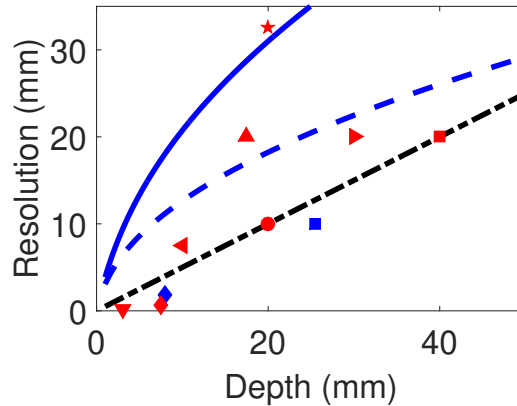


Fig. 2.1. Resolution of diffuse optical imaging as reported in the literature. Red symbols are image reconstructions, where \blacktriangledown , \blacklozenge , \blacktriangleleft , \blacktriangle , \bullet , \star , \blacktriangleright , and \blacksquare , correspond to [34–37, 45–48]. Blue symbols are solution measurements (no inversion was performed), \blacklozenge and \blacksquare correspond to [32, 49]. The background μ'_s and μ_a used in each paper varies, but their average values are 0.85 mm^{-1} and 0.0063 mm^{-1} (close to those of tissue-simulating Intralipid), where μ'_s is between 0.5 and 1.0 mm^{-1} and μ_a is between 0 and 0.01 mm^{-1} . The blue curves are theoretical resolution limits for CW ($\omega = 0$) direct measurements, as calculated by Ripoll *et al.* [33]. The dashed blue curve was calculated using breast tissue parameters, where $\mu'_s = 1.5 \text{ mm}^{-1}$ and $\mu_a = 0.0035 \text{ mm}^{-1}$. The solid blue curve was calculated using the average values from the literature. The black curve is $\text{depth}/2$.

proved through localization, where the problem becomes finding the position of a point source [19–21]. The prior information that is incorporated into the inversion is that a measurement data set contains information about only a single fluorescent inhomogeneity. Practically, such measurements could be made, for example, if the inhomogeneities have sufficient separation in space, time, and/or emission spectrum. Furthermore, we model every inhomogeneity as a point source, an assumption that has been shown to be valid numerically and experimentally for fluorescent inhomogeneities with diameters up to 10 mm at depths of 10-20 mm in tissue-simulating 1 % Intralipid [21]. This assumption holds because of the rapid attenuation of high spatial frequencies within the scattering medium. Here, the efficacy of localizing a cylindrical fluorescent inhomogeneity with 1 mm diameter and 2 mm height is demonstrated. With sufficient SNR, smaller inhomogeneities could be localized, and previous work [21] suggests that larger inhomogeneities with diameters of at least 10 mm could also be localized. If needed, the forward model could be modified for structured or larger inhomogeneities, extending localization beyond a single point in space.

2.2 Localization

We propose localization as a means for finding fluorescent inhomogeneities embedded within a highly scattering medium with great precision. The method estimates the location of an inhomogeneity by fitting measured intensity data to a diffusion equation forward model for a point emitter, allowing extraction of the 3-D position of the inhomogeneity. For the forward model, we use an analytical solution to the diffusion equation in an infinite slab geometry [1], and we note that analytical solutions can be derived for more complicated geometries [52], or the forward model could be solved using a numerical method [53].

2.2.1 Forward Model

Equations (2.1) and (2.2) can be used to derive a forward model for comparison with measured data. For experimental simplicity, we set $\omega = 0$, so that the data is an integration over the measured temporal response at each measurement location. As seen in Fig. 2.2, a single point excitation source corresponding to the laser excitation is positioned at \mathbf{r}_s . In this case, $S_x(\mathbf{r}, \omega) = S_o \delta(\mathbf{r} - \mathbf{r}_s)$, where S_o is the laser excitation power density (W/mm³) and δ is the Dirac delta function. Furthermore, N point detectors at λ_m that correspond to camera pixels behind an emission band-pass filter are placed at positions \mathbf{r}_i , where i is an index from 1 to N . Finally, in the example we consider, a single fluorescent point source is located at \mathbf{r}_f , such that $S_f(\mathbf{r}, \omega) = \eta \mu_{a_f} \delta(\mathbf{r} - \mathbf{r}_f)$, where η is the fluorophore's quantum yield and μ_{a_f} is its absorption. Estimating \mathbf{r}_f constitutes localization. Under these conditions, we let $g_x(\mathbf{r}_s, \mathbf{r}_f)$ represent the Green's function for (2.1) at λ_x (the excitation wavelength) and $g_m(\mathbf{r}_f, \mathbf{r}_i)$ be the Green's function for (2.2) at λ_m (the fluorescent wavelength), assuming an infinite slab geometry. Then, the i th element of the forward model vector, describing the fluorescence emission measured at \mathbf{r}_i , \tilde{f}_i , is

$$\tilde{f}_i(\mathbf{r}_f) = w [g_m(\mathbf{r}_f, \mathbf{r}_i) g_x(\mathbf{r}_s, \mathbf{r}_f)] \quad (2.4)$$

$$\equiv w f_i(\mathbf{r}_f), \quad (2.5)$$

where w is a multiplicative constant that incorporates η , S_o , and the efficiency of light coupling into the medium, and $f_i(\mathbf{r}_f)$ depends nonlinearly on \mathbf{r}_f . The excitation laser light incident upon the medium is approximated in the model as an isotropic point source located one mean-free path length ($l^* = 3D$) into the medium [1, 11, 21], where l^* is the distance for photon momentum randomization. Similarly, the light collected by the detectors, in our case each pixel of a camera, is modeled as that given by a diffusion model at points located l^* into the medium. We derive f_i using the extrapolated zero flux boundary conditions shown in Fig. 2.2 to simulate an infinite homogeneous slab geometry [1]. The extrapolated boundary condition can accommodate mismatched background refractive indices at the surface. We set

the extrapolated boundary $l_s = 5.03D$ away from the physical surface, analogous to an interface between air and scatterers in water [54] and useful in our earlier experiments [21], to approximately model the physical boundary for the experimental results we present. Four pairs of excitation and fluorescent image sources are placed to approximately enforce $\phi = 0$ at the extrapolated boundary. Superposition of the physical and image sources allows analytic expressions for $g_x(\mathbf{r}_s, \mathbf{r}_f)$ and $g_m(\mathbf{r}_f, \mathbf{r}_i)$ to be obtained that have the form in (2.3).

2.2.2 Position Estimation

If a fluorescent inhomogeneity is present, which can be determined subject to some probability of detection [21], in order to localize it, we must estimate \mathbf{r}_f . This can be accomplished through minimization of the cost function

$$c(\mathbf{r}_f) = \min_w \|\mathbf{y} - w\mathbf{f}(\mathbf{r}_f)\|_{\mathbf{\Upsilon}^{-1}}^2 \quad (2.6)$$

over all \mathbf{r}_f of interest, where \mathbf{y} is a vector of N measurements, $\mathbf{f}(\mathbf{r}_f)$ is a vector of N normalized forward calculations $f_i(\mathbf{r}_f)$, from (2.5), $\mathbf{\Upsilon} = \alpha \text{diag}[|y_1|, \dots, |y_N|]$ is the noise covariance matrix, for which we assume a Gaussian noise model characterized by α [11], and for an arbitrary vector \mathbf{v} , $\|\mathbf{v}\|_{\mathbf{\Upsilon}^{-1}}^2 = \mathbf{v}^H \mathbf{\Upsilon}^{-1} \mathbf{v}$, where H denotes the Hermitian transpose. A two step procedure can be used to solve this optimization problem [21, 55], where the minimization in (2.6) with respect to w leads to

$$\tilde{w}(\mathbf{r}_f) = \frac{\mathbf{f}^T(\mathbf{r}_f) \mathbf{\Upsilon}^{-1} \mathbf{y}}{\mathbf{f}^T(\mathbf{r}_f) \mathbf{\Upsilon}^{-1} \mathbf{f}(\mathbf{r}_f)}, \quad (2.7)$$

found by taking the derivative with respect to w and setting the result equal to zero, and this estimate results in the modified cost function

$$c(\mathbf{r}_f) = \|\mathbf{y} - \tilde{w}(\mathbf{r}_f) \mathbf{f}(\mathbf{r}_f)\|_{\mathbf{\Upsilon}^{-1}}^2. \quad (2.8)$$

The maximum likelihood estimates are then

$$\hat{\mathbf{r}}_f = \arg \min_{\mathbf{r}_f} c(\mathbf{r}_f) \quad (2.9)$$

$$\hat{w} = \tilde{w}(\hat{\mathbf{r}}_f), \quad (2.10)$$

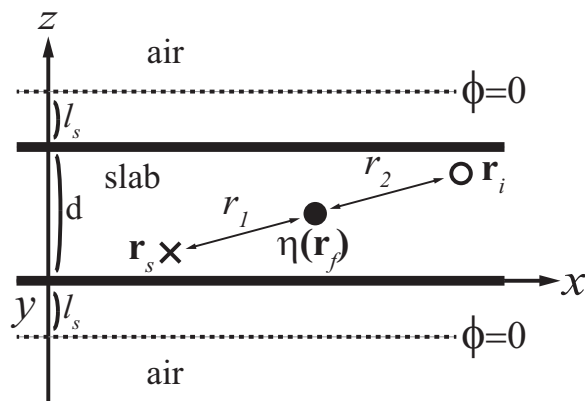


Fig. 2.2. Model geometry for an infinite slab of thickness d , where $\mathbf{r} = (x, y, z)$. An excitation source (X) at \mathbf{r}_s and a fluorescence emission detector (O) at \mathbf{r}_i are placed one scattering length $l^* = 3D$ away from the slab boundaries as shown. A fluorescence source (\bullet) is at the unknown position \mathbf{r}_f . Zero flux ($\phi = 0$) boundary conditions with $l_s = 5.03D$ are used to simulate an infinite slab geometry [21].

where (2.8) is minimized over a set of values for \mathbf{r}_f bounded by the slab geometry. Therefore, the estimate $\hat{\mathbf{r}}_f$ in (2.9) is the position within the slab that returns the lowest value of the cost function (2.8). In our illustrative example of a homogeneous scattering slab, this minimization can be computed quickly because the Green's functions from (2.4) used to calculate $\mathbf{f}(\mathbf{r}_f)$ are closed-form and given by (2.3). However, the forward model data could also be generated using finite element or related numerical methods [53], at the cost of increased computational time.

We use simulations of solution measurements in Fig. 2.3 to demonstrate the localization of a fluorescent source in a slab. Figure 2.3(a) shows the problem geometry where the positions of an excitation source, a fluorescent source, and $N = 400$ detectors are shown as red, green, and blue points, respectively. We let \mathbf{r}_{ft} be the true location of the fluorescent source. The slab is 18 mm thick with $\mu_a = 0$ and $\mu'_s = 0.9 \text{ mm}^{-1}$. The localization procedure was performed on the discretized region of interest ($2 \times 2 \times 1.8 \text{ cm}^3$) with $N_x = 17$ points in the x dimension, $N_y = 17$ points in the y dimension, and $N_z = 17$ points in the z dimension. Following the localization procedure, $\tilde{w}(\mathbf{r}_f)$ from (2.7) and then $c(\mathbf{r}_f)$ from (2.8) were evaluated at each grid point in the region of interest. Figures 2.3(b) and (c) show plots of $\tilde{w}(\mathbf{r}_f)$ and $c(\mathbf{r}_f)$ for a fixed y that contains the minimum of $c(\mathbf{r}_f)$. $\hat{\mathbf{r}}_f$ and \hat{w} are then calculated using (2.9) and then (2.10). We calculated the localization error as $[(\mathbf{r}_{ft} - \hat{\mathbf{r}}_f)/\mathbf{r}_{ft} \times 100]\%$. The localization error in Fig. 2.3 is high because of the course discretization over the region of interest. In Section 2.2.3, we present a computationally efficient method for removing the discretization error.

2.2.3 Multigrid for Super Resolution

In order to achieve high resolution, the grid spacing of the points within the region of interest must be reduced from what is used in Figs. 2.3(a) and (b). However, this presents a computational problem when evaluating $\tilde{w}(\mathbf{r}_f)$ and $c(\mathbf{r}_f)$, because (2.4) must be calculated for each combination of \mathbf{r}_i and \mathbf{r}_f within the region of interest.

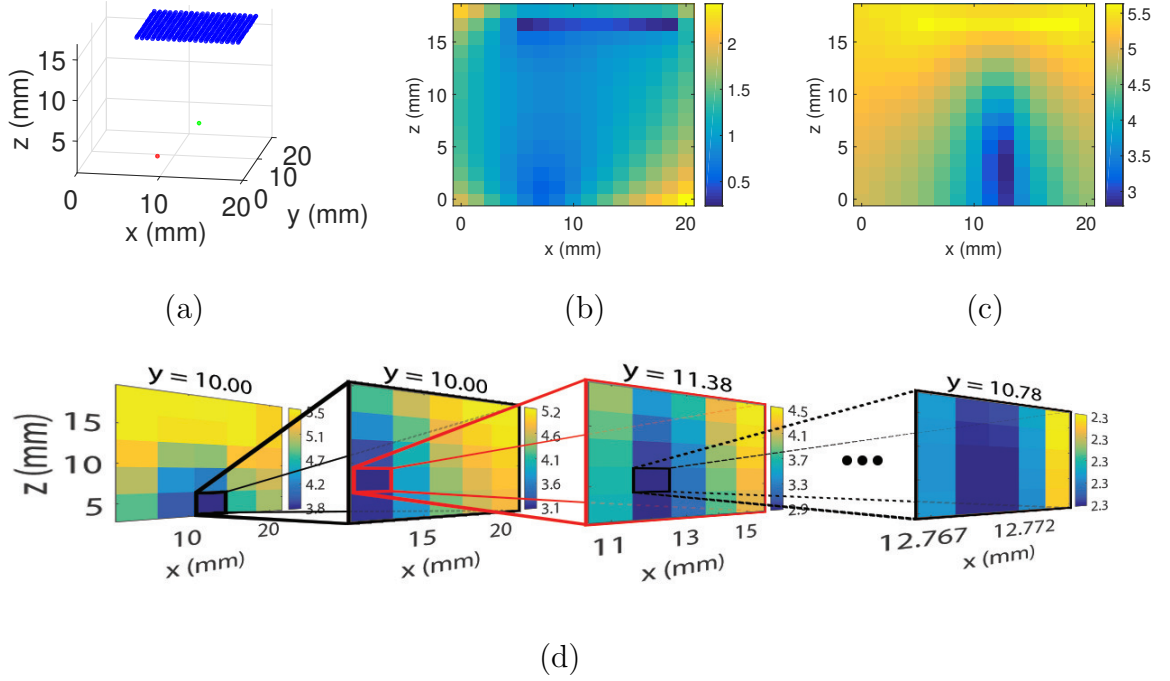


Fig. 2.3. Slab problem geometry and a demonstration of the localization of a point fluorescent source with high discretization error. (a) Slab problem geometry with $\mathbf{r}_s = (8.09, 9.07, 1.11)$ mm plotted as the red point, $\mathbf{r}_{ft} = (12.77, 10.79, 5.0)$ mm plotted as the green point, and $N = 400$ detector locations \mathbf{r}_i plotted as blue points. The slab is 18 mm thick with $\mu'_s = 0.9 \text{ mm}^{-1}$ and $\mu_a = 0 \text{ mm}^{-1}$. These positions were used so that the simulation and experimental results can be compared. The slab has the same dimensions and properties as used in the experiment. Measurements were simulated using (2.4) with $w = 10$ and a 30 dB SNR, and $\tilde{w}(\mathbf{r}_f)$ from (2.7) and $c(\mathbf{r}_f)$ from (2.8) were evaluated over the region of interest. (b) Plot of $\tilde{w}(\mathbf{r}_f)$ slice and (c) plot of $c(\mathbf{r}_f)$ slice for fixed y , such that the plots contains the point that minimizes $c(\mathbf{r}_f)$. Here, $y = 10.59$, and the color bars have log scales with arbitrary units. Using (2.9), $\hat{\mathbf{r}}_f = (12.94, 10.59, 5.29)$, and using (2.10), $\hat{w} = 10.07$. The localization errors in the x , y , and z dimensions are 1.37%, 1.85%, and 5.88%, respectively. The course discretization of the region of interest is a primary contributor to the estimation error. (d) Localization with multiresolution. Plots of $c(\mathbf{r}_f)$ slices for fixed y are shown for multiresolution iterations 1, 2, 3, and 13. At iteration 13, from (2.9), $\hat{\mathbf{r}}_f = (12.77, 10.78, 4.98)$, and from (2.10), $\hat{w} = 10.02$. The localization errors in the x , y , and z dimensions are 0.05%, 0.05%, and 0.19%, respectively. The discretization error has been minimized.

For this reason, we apply a multiresolution method to simultaneously reduce the computational time and the discretization error of the localization. This multiresolution approach is similar to multigrid in the general sense that it incorporates a hierarchy of discretization grids into the localization [56, 57]. However, multigrid algorithms propagate solutions back and forth between coarse and fine grids to reduce errors, whereas our multiresolution approach iterates strictly in one direction from coarse to finer grids. Therefore, we use the term multiresolution to describe the method, which is demonstrated in Fig. 2.3(d). First, the cost $c(\mathbf{r}_f)$ is calculated and minimized in the region of interest with dimensions $2 \times 2 \times 1.8 \text{ cm}^3$, as before, but with a grid of $N_x = N_y = N_z = 5$. The cost is then iteratively calculated on successively smaller regions of interest that each encompass the point of minimum cost found from the previous iteration. At each iteration after the first, the region of interest extends a distance equal to the grid spacing of the previous iteration along each dimension around the point of minimum cost, and the grid contains the same number of grid points ($5 \times 5 \times 5$). This procedure is repeated until convergence, which we defined as two grids where the change in the minimum cost was less than 0.1%, but not equal to zero. In Fig. 2.3(d), the first three iterations are shown. It is observed that successive iterations appear to “zoom in” on the point of lowest cost. After 13 iterations, the convergence condition was satisfied and $\hat{\mathbf{r}}_f$ was calculated using (2.9). The localization error is much less than that of Fig. 2.3(b) and (c) because multiresolution has effectively minimized the discretization error.

2.3 Results

We use the multigrid localization method described in Section 2.2 to achieve SR-DOI. The potential for super-resolution is perhaps apparent in Fig. 2.3(d), but the limits on the resolution are not clear. Here, we evaluate these limits using numerical simulation and experimental validation.

2.3.1 Simulation

A Gaussian noise model is implied by (2.6), and the use of non-zero elements only on the diagonal of $\mathbf{\Upsilon}$ is a consequence of the assumption of independent measurements. The model assumes that each measurement is normally distributed with a mean equal to the noiseless measurement and a variance that is proportional to the DC ($\omega = 0$) component of the noiseless measurement [11]. Simulated noisy data can therefore be numerically generated as

$$y_i = \tilde{f}_i(\mathbf{r}_f) + [\alpha|\tilde{f}_i(\mathbf{r}_f)|]^{1/2} \times N(0, 1), \quad (2.11)$$

where $N(0, 1)$ is a zero mean Gaussian random variable with unit variance, and α scales the noise variance. The signal-to-noise ratio (SNR in dB) at the i th detector is then

$$\text{SNR}_i = 10 \log_{10} \left(\frac{1}{\alpha} |\tilde{f}_i(\mathbf{r}_f)| \right). \quad (2.12)$$

This noise model assumes that the uncertainty in the estimated position of the fluorescent inhomogeneity ($\hat{\mathbf{r}}_f$) is dominated by measurement noise. This would not be the case, for example, if the fluorophores changed position or diffused significantly during the integration time of the measurement [58, 59].

Since the measurements are noisy, each localized position $\hat{\mathbf{r}}_f$ falls within an underlying probability distribution function $p(\mathbf{r}_f)$ with true mean $\mu = \mathbf{r}_{ft}$ and variance σ^2 . The performance of the localization can therefore be evaluated by estimating σ , which has been called the localization uncertainty [58–62]. By the central limit theorem, σ can be estimated from a sufficient number of samples of $p(\mathbf{r}_f)$ [63]. Here, we calculate $\hat{\sigma}_x$, $\hat{\sigma}_y$, and $\hat{\sigma}_z$, which are estimates of σ corresponding to each of the xyz coordinates of \mathbf{r}_f . We use the same geometry, optical properties, \mathbf{r}_s , \mathbf{r}_i , and \mathbf{r}_f as in Fig. 2.3 to generate samples of $p(\mathbf{r}_f)$.

First, we generated 50 noisy independent solution measurements for an assumed SNR using (2.11). Each simulated measurement data set was then used to determine $\hat{\mathbf{r}}_f$ using (2.9) with multiresolution. Finally, $\hat{\sigma}_x$, $\hat{\sigma}_y$, and $\hat{\sigma}_z$, were calculated from the 50 values of $\hat{\mathbf{r}}_f$. The results from this statistical analysis are shown in Fig. 2.4(a).

The depth of the fluorescent inhomogeneity, or its distance from the detector plane, was 13 mm, as shown in Fig. 2.3. Figure 2.4(a) gives plots of $\hat{\sigma}_x$, $\hat{\sigma}_y$, and $\hat{\sigma}_z$ versus SNR, and Fig. 2.4(b) shows a subset of this data as ellipses, where the major and minor axes have dimension $4\hat{\sigma}_x$ or $4\hat{\sigma}_y$. We chose $4\hat{\sigma}_x$ and $4\hat{\sigma}_y$ to indicate the space containing 95% of the localized points. Figure 2.4(c) presents plots of $\hat{\sigma}_x$, $\hat{\sigma}_y$, and $\hat{\sigma}_z$ versus depth for a constant SNR of 30 dB, and Fig. 2.4(d) shows plots of ellipses for different depths. It is clear that $\hat{\sigma}_z$ is consistently larger than $\hat{\sigma}_x$ and $\hat{\sigma}_y$. This occurs because the detectors are on a constant z -plane. The value of $\hat{\sigma}_z$ could be reduced to the levels of $\hat{\sigma}_x$ and $\hat{\sigma}_y$ by placing additional detectors in the $x - z$ or $y - z$ planes. Thus, $\hat{\sigma}_x$ and $\hat{\sigma}_y$ are better indicators of the achievable localization uncertainty for the geometry in Fig. 2.3(a). The reason $\hat{\sigma}_x$ does not equal $\hat{\sigma}_y$ and the ellipses are not perfect circles is because of the uncertainty in the estimations and the fact that the 400 detectors locations in Fig. 2.3(a) are not perfectly symmetric around the fluorescent inhomogeneity. Even though we use the same equation for the forward model that was used to generate the simulated data, it is not guaranteed that the localization will work due to the addition of simulated noise. In the next section we will validate our localization scheme with experimental data and demonstrate that the simulated results closely match those from the experiment.

2.3.2 Experiment

We present the results of an experimental study of the accuracy of SRDOI with measurement data collected using the arrangement shown in Fig. 2.5(a). A highly scattering slab of thickness $d = 18$ mm was created by stacking three pieces of white plastic (Cyro Industries, Acrylite FF, a clear acrylic with 50 nm TiO_2 scatterers) with dimensions $140 \times 140 \times 6$ mm. A hole with a diameter of 1 mm and a depth of 2 mm was drilled into the top-center of the bottom slab. The size of this hole is large relative to the expected localization uncertainty, however it is small enough to be well approximated by a fluorescent point source in a heavily scattering medium [21]. A

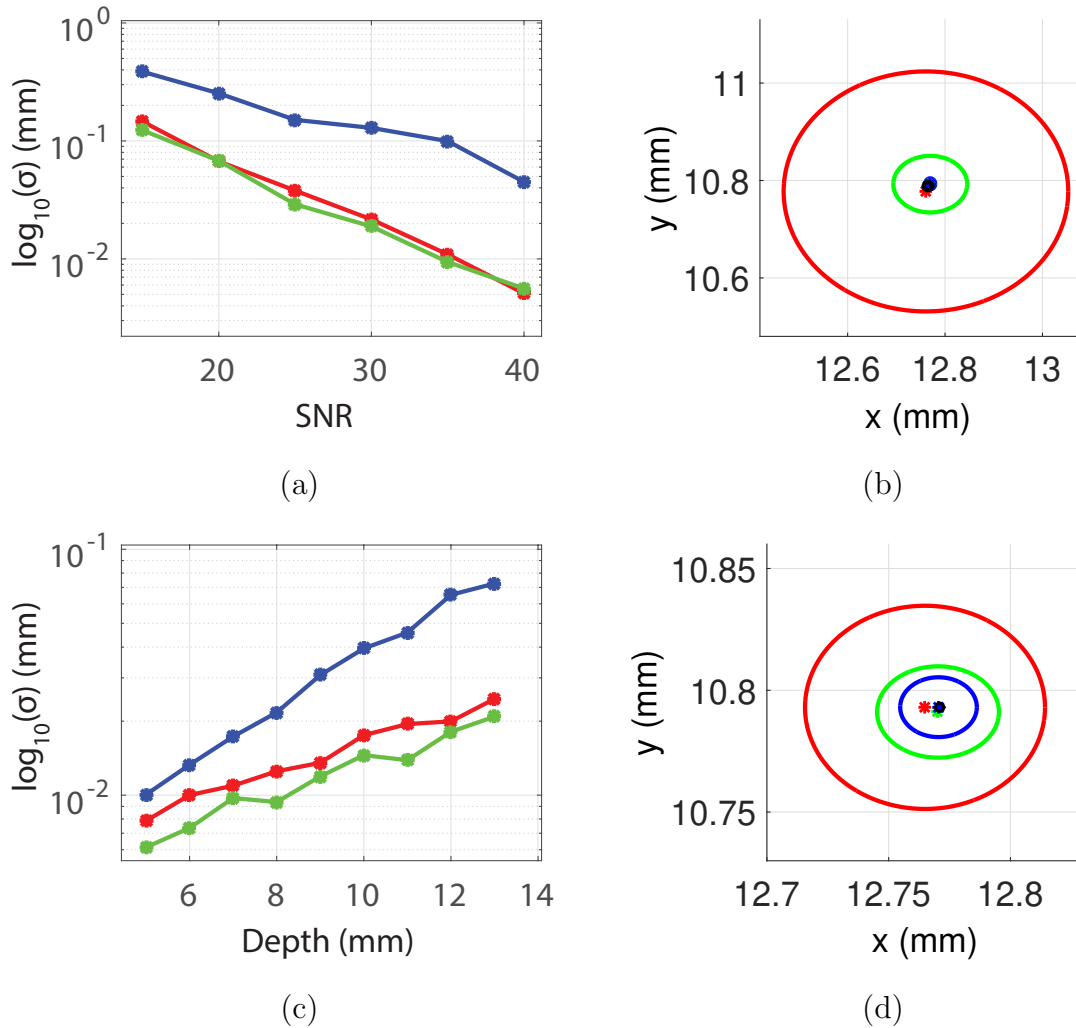


Fig. 2.4. Uncertainty in the numerical localization of a fluorescent inhomogeneity in the slab geometry shown in Fig. 2.3(a). The standard deviations were estimated using 50 noisy independent measurements that were generated using (2.11). (a) $\hat{\sigma}_x$, $\hat{\sigma}_y$, and $\hat{\sigma}_z$ versus SNR plotted as red, green, and blue curves, respectively. The depth of the fluorescent inhomogeneity was 13 mm, as shown in Fig. 2.3(a). $\hat{\sigma}_z$ is larger than $\hat{\sigma}_x$ and $\hat{\sigma}_y$ because the detectors are only in the $x - y$ plane. (b) Ellipses in the $x - y$ plane with major and minor axes of lengths $4\hat{\sigma}_x$ or $4\hat{\sigma}_y$ and means given by their center point. Red, green, and blue ellipses correspond to SNRs of 15 dB, 25 dB, and 40 dB, respectively. (c) $\hat{\sigma}_x$, $\hat{\sigma}_y$, and $\hat{\sigma}_z$ versus depth plotted as red, green, and blue curves, respectively, with 30 dB SNR. (d) Ellipses in the $x - y$ plane with major and minor axes of length $4\hat{\sigma}_x$ or $4\hat{\sigma}_y$ and means given by their center point. Red, green, and blue ellipses correspond to depths of 13 mm, 8 mm, and 5 mm, respectively.

10 mM stock of the fluorophore Maleimide ATTO 647N (peak $\lambda_x = 646$ nm, peak $\lambda_m = 664$ nm) in dimethyl sulfoxide (DMSO) was used to prepare a 10 μ M diluted solution of the fluorophore. This fluorophore solution was carefully placed into the drilled hole in the bottom highly scattering slab using a pipette and a needle to remove air bubbles.

The filtered output of a pulsed supercontinuum source (EXR-20 NKT Photonics, 5 ps seed pulse width, 20 MHz repetition rate, VARIA tunable filter) was used to generate the excitation light at $\lambda_x = 633$ nm with a 10 nm bandwidth, as shown in Fig. 2.5(a). With this bandwidth, the average excitation power was approximately 15 mW. Measurements at $\lambda_m = 676$ nm were made through an OD6 bandpass filter having a bandwidth of 29 nm (Edmund Optics 86-996), to reject the excitation light. Measurements at λ_x were performed by removing the bandpass filter. All measurements were pseudo-CW (corresponding to unmodulated light data and $\omega = 0$ in (2.1) and (2.2)), with the CCD camera (PIMAX, 512 x 512 pixels) integration time being long compared to the pulsed laser repetition rate (20 MHz). A λ_x measurement result with an integration time of 30 ms is shown in Fig. 2.5(b).

All λ_m measurements were calibrated by subtracting corresponding measurements of the filter bleed-through, according to $y_i = y_i^{slab} - y_i^{bleed}$, where y_i is the i th component of \mathbf{y} , y_i^{slab} is the i th experimental datum captured from the slab, and y_i^{bleed} is the i th experimental datum from the slab without the fluorescent inhomogeneity present. A calibrated λ_m measurement with an integration time of 1 s is shown in Fig. 2.5(c). We selected $N = 400$ detector locations (pixels) around the maximum value, as shown by the blue dots. The values (indicated by the color bar) at these positions were used to construct the data vector \mathbf{y} in (2.6).

In order to calculate the forward solution in (2.4), μ'_s , μ_a , \mathbf{r}_i for each detector along with \mathbf{r}_s must be known. To determine these, first the positions of all pixels in Fig. 2.5(b) and (c) were found in mm using images of a ruler like that shown in Fig. 2.5(d). Care was taken in the alignment of the experimental components so that the distance between each pixel in the x and y dimensions was approximately

the same (0.043 mm). The x_i and y_i coordinates of the vector \mathbf{r}_i could then be determined from the positions of the chosen 400 detector pixels, and the z coordinate was $(18 - 3D)$ mm, to satisfy the zero-flux boundary condition at the top of the scattering medium [1]. The point directly below the maximum intensity in Fig. 2.5(b) indicates the source position, \mathbf{r}_s . This position of maximum intensity was estimated by fitting a 2-D Gaussian function [58] to Fig. 2.5(b). This procedure resulted in $\mathbf{r}_s = (8.09, 9.07, 3D)$ mm, where the z component is $3D$ to satisfy the boundary condition at the bottom of the scattering medium [1]. The 2-D Gaussian fit was also used to estimate the true location of the fluorescent inhomogeneity using a data set with 50 times the integration time of that used for Fig. 2.5(c), resulting in a much higher SNR than that of Fig. 2.5(c). The true location was estimated as the centroid with coordinates $\mathbf{r}_{ft} = (12.77, 10.79, 5.0)$ mm, where the z component at the center of the drilled hole was found from the thickness of the white plastic slabs (6 mm) and the depth of the drilled hole (2 mm). We note that the 2-D Gaussian fit does not provide depth information, motivating the use of the localization method in Section 2.2 even in this simple example.

The optical parameters of the slab, μ'_s and μ_a , were estimated by fitting (2.3) to the data shown in Fig. 2.5(b), where in this case, $\mathbf{r}' = \mathbf{r}_s$, $\mathbf{r} = \mathbf{r}_i$, and the z components of \mathbf{r}_s and \mathbf{r}_i depended on μ'_s and μ_a . The data in Fig. 2.5(b) was captured with the fluorescent inhomogeneity present, but because the bandpass filter used in the experiment attenuated the excitation light by a factor of 10^6 , the fluorescent signal in Fig. 2.5(b) was assumed to be negligible compared to the transmitted excitation light. It was also assumed that the scattering medium background exists throughout the small volume occupied by the fluorophore. The scattering slabs used have very low absorption in the wavelength range for these experiments, so we set $\mu_a = 0$. The estimated μ'_s of the slab (at 633 nm) was found to be 0.9 mm^{-1} , giving $3D = 1.111$ mm. These values are within the uncertainty of previous estimates using the same method [64]. The positions \mathbf{r}_s , \mathbf{r}_i , and \mathbf{r}_{ft} , are those indicated in Fig. 2.3, and

were used for the corresponding numerical simulations in Section 2.2 and Fig. 2.4, so that the simulation and experimental results can be compared.

The forward solution calculated in (2.4) using the experimental parameters, along with the experimental measurement vector \mathbf{y} , allow localization of the fluorescent inhomogeneity embedded in the highly scattering slab. In order to characterize the experimental localization uncertainty, the λ_m measurement shown in Fig. 2.5(c) was repeated 50 times. Localization using these 50 measurements then allows calculation of the experimental $\hat{\sigma}_x$, $\hat{\sigma}_y$, and $\hat{\sigma}_z$. The resulting values are shown plotted as an ellipse in Fig. 2.6(a), with an axial ratio of $\hat{\sigma}_y/\hat{\sigma}_x = 0.0232/0.0229$ (i.e., close to circular), and presented in Table 2.1.

In order to validate the SRDOI method, the experimental results in Fig. 2.6(a) can be compared to the numerical data in Fig. 2.4. These results were all generated using the same \mathbf{r}_s , \mathbf{r}_i , and \mathbf{r}_{ft} , and identical scattering medium optical parameters, μ'_s and D . In order to estimate the SNR of the experiment, we calculated the ML estimate of the noise parameter α from the full form of (2.6) [57], giving

$$\hat{\alpha} = \frac{1}{N} \|\mathbf{y} - \hat{w}\mathbf{f}(\hat{\mathbf{r}}_f)\|_{\tilde{\mathbf{Y}}^{-1}}^2, \quad (2.13)$$

where $\tilde{\mathbf{Y}} = \text{diag}[|y_1|, \dots, |y_N|]$ uses measured data. The SNR of the i th detector was then estimated using (2.12) as

$$\text{SNR}_i = 10 \log_{10} \left(\frac{1}{\hat{\alpha}} |\hat{w} f_i(\hat{\mathbf{r}}_f)| \right). \quad (2.14)$$

The SNR was calculated for all 400 detectors using (2.14) and one of the 50 experimental data sets and its corresponding values for \hat{w} and $\hat{\mathbf{r}}_f$. The mean experimental SNR was found to be 28.9 dB, its standard deviation across detectors was 0.62 dB, and its maximum was 29.9 dB. We used this mean SNR to generate the blue ellipse in Fig. 2.6(b), which is plotted with the red ellipse from Fig. 2.6(a). The values for the numerical localization uncertainties are also presented in Table 2.1. Note that the experimental and numerical uncertainties are close, signifying that (2.12) describes the noise process well. The difference between the experimental mean and the true

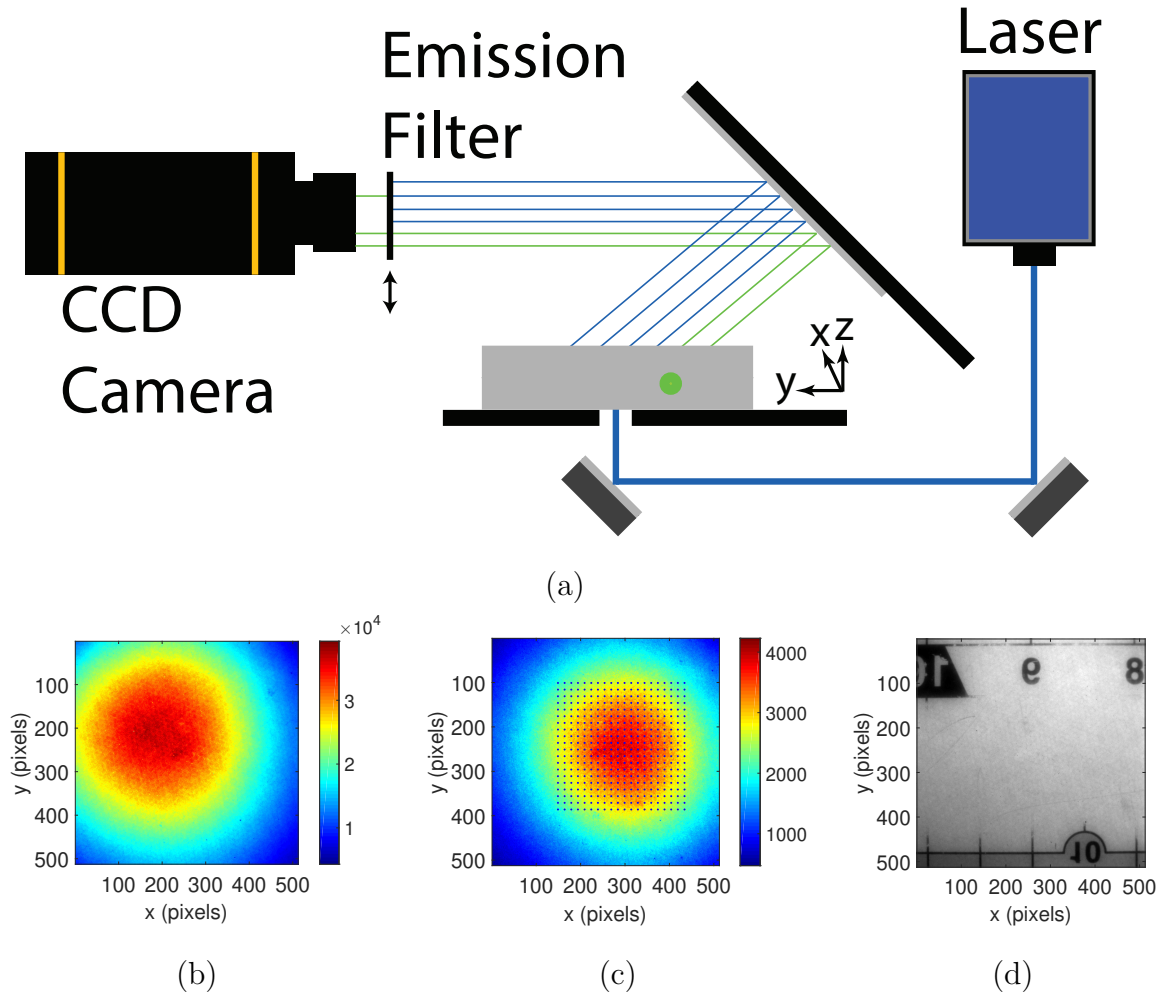


Fig. 2.5. (a) Experiment setup for localization of a fluorescent inhomogeneity (green point). The fluorescent inhomogeneity (ATTO 647N) is embedded in a highly scattering slab that is 18 mm thick. The laser source is a filtered pulsed supercontinuum source (EXR-20 NKT Photonics, 5 ps seed pulse width, 20 MHz repetition rate, VARIA tunable filter). The laser source is tuned to λ_x , and detection is by a CCD camera with or without a bandpass filter at λ_m . (b) Light at λ_x detected by the CCD camera without the bandpass filter. Because the bandpass filter attenuates the excitation light by a factor of 10^6 , the fluorescent signal is negligible compared to the transmitted excitation light when the bandpass filter is not used. (c) Light at λ_m (after background subtraction) detected by the CCD camera with the bandpass filter. The positions of the 400 detectors are shown as blue dots. (d) CCD image of a ruler showing the field of view (about 22.02 mm by 22.02 mm). Images of the ruler were used to convert pixels to mm.

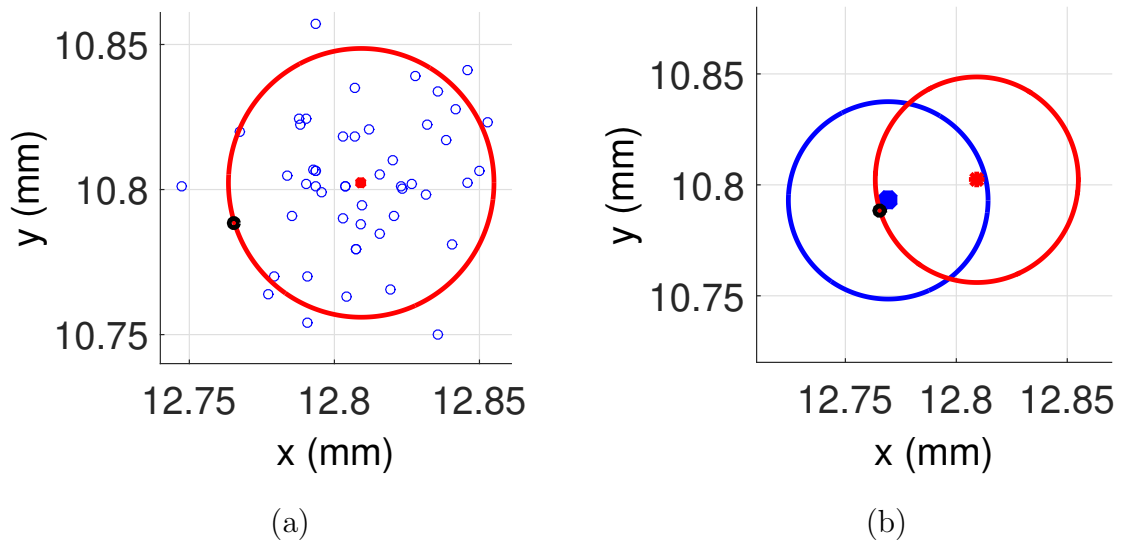


Fig. 2.6. Experimental localization uncertainty for the fluorescent inhomogeneity embedded in the highly scattering slab of Fig. 2.5. Experimental values for $\hat{\sigma}_x$, $\hat{\sigma}_y$, and $\hat{\sigma}_z$ were estimated using 50 independent experimental measurements. (a) Plot of the (x, y) components of the localized positions as blue points. These points were used to calculate the major and minor axes of the red ellipse, which have dimensions $4\hat{\sigma}_x$ or $4\hat{\sigma}_y$, as well as its center red point, which is the mean. The black point is the true location that was estimated with a 2-D Gaussian fit. (b) Comparison of the experimental uncertainty to the numerical uncertainty. The blue ellipse was generated from numerical data with mean SNR= 28.9 dB to match the experimental value, and the red ellipse is the same as in (a). See Table 2.1 for the numerical values.

location is likely due to the fit approximation used to determine the true location and estimation error.

2.3.3 Resolution

A natural way to compare the localization uncertainties to the resolution of diffuse optical imaging is to calculate the FWHM of the density function $p(\mathbf{r}_f)$ that describes the localized positions. For a localization uncertainty σ and a Gaussian spread of localized points, we can write the resolution as

$$\text{Resolution} = 2\sqrt{2\ln 2} \sigma \approx 2.36 \sigma, \quad (2.15)$$

corresponding to the full width at one half of the maximum. The numerical and experimental results are summarized in Table 2.1 for the case of depth = 13 mm, as shown in Fig. 2.3, and a mean SNR of 28.9 dB, found for the experiment. The $\hat{\mu}_x$, $\hat{\mu}_y$, and $\hat{\mu}_z$ are the mean of the localized position components. The FDOT resolution is estimated as depth/2.

2.4 Conclusion

We have developed a localization method that allows imaging of fluorescent inhomogeneities deep in heavily scattering media with unprecedented spatial resolution. The method was validated numerically and experimentally, demonstrating an improvement of two orders of magnitude in resolution compared to DOI. Alternatively, numerical methods such as the finite element method could be used to solve the forward problem for inhomogeneous media, where DOT could be employed to determine μ'_s and μ_a [65, 66]. However, the limited resolution to which μ'_s and μ_a could be estimated with DOT in inhomogeneous media may increase the localization uncertainty. The localization constraints could be incorporated into the FDOT framework [15, 67], potentially allowing reconstruction of super-resolution images. Also, (2.6) could be minimized using alternative optimization methods, such as a gradient search.

Table 2.1.

Estimated numerical and experimental localization uncertainties, means, and resulting resolution (mm). The resolution of FDOT is assumed to be depth/2.

	SRDOI Numerical	SRDOI Experimental	FDOT
$(\hat{\sigma}_x, \hat{\sigma}_y, \hat{\sigma}_z)$	(0.0225, 0.0222, 0.1301)	(0.0229, 0.0232, 0.1089)	–
$(\hat{\mu}_x, \hat{\mu}_y, \hat{\mu}_z)$	(12.769, 10.793, 4.972)	(12.809, 10.802, 4.875)	–
Resolution	(0.0530, 0.0523, 0.3064)	(0.0539, 0.0546, 0.2564)	6.5

The diffusion model presented in (2.1) and (2.2) assumes that the photon current density does not change over one transport mean free path, $l^* = 3D$. For the white plastic slab used here, $l^* = 1.11$ mm at 633 nm, which is much larger than the localization uncertainties in Table 2.1. Therefore, SRDOI can find a fluorescent inhomogeneity with a resolution that is much less than the minimum length described by the physics in the diffusion model. This is possible because of the prior information that has been incorporated into the localization. The results suggest that the localization uncertainty is dominated by measurement noise and not inaccuracies in the model. Therefore, a more accurate model, such as the radiative transfer equation (RTE), is not required unless the combination of the diffusion equation forward model and the prior information is insufficient for accurate localization. This could be the case with weak scatter or high absorption, for example.

We found that a single excitation source position, \mathbf{r}_s , was sufficient for the situation considered, which is practical for experimentation. However, multiple excitation source positions or expanded beam excitation may increase the fluorescence emission and reduce the localization uncertainty. A low-pass spatial filter could be applied to the experimental data before estimating \mathbf{r}_f in order to further reduce the localization uncertainty (results not shown). This would smooth the noisy experimental data prior to the localization. The computational time could be reduced and the experiment simplified by using fewer detectors [21]. A few sensitive photodetectors placed at the surface of a scattering medium should be sufficient to localize an inhomogeneity with higher SNR than what can be achieved with a CCD camera. Figure 2.5(a) shows a transmission measurement, but a reflection measurement could be performed.

Practical application of SRDOI requires access to fluorescent light data that can be assumed to originate from single fluorescent inhomogeneities. This could be accomplished through known variations in space, time, the fluorescence emission spectrum, or a combination of these. Variation in space could simply be fluorescent inhomogeneities separated by distances greater than the FWHM of the PSF. Variation in time could be a unique temporal delay for each inhomogeneity, where measurements

with short integration times (and sufficient SNR) could allow separation of the temporal responses. Finally, if each inhomogeneity emitted photons at different energies, a spectral measurement could allow separation of each response. All of these variations are possible with blinking quantum dots of different diameters [68], where each quantum dot could then be localized in deep tissue.

Localization techniques have also been developed in microscopy for improving resolution [26, 61]. For example, in stochastic optical reconstruction microscopy (STORM) [27], a subset of fluorescent molecules that are separated by a distance greater than the diffraction limit are switched between fluorescent and non-fluorescent states. Each molecule is then located with an uncertainty that is much less than the diffraction limit. With multiple measurements, a super-resolution image is formed by combining many localized positions. However, this is a fundamentally different class of problem where scatter is largely ignored and the imaging system objective function is incorporated into the localization framework. In our case, a model for the heavily scattering domain is used in an optimization-based localization framework. Interestingly, the improvement in spatial resolution that is achieved with super-resolution in microscopy is comparable to what is achieved by SRDOI. For example, a diffraction-limited resolution of 200 nm is improved to a few nanometers when imaging single fluorescent molecules [69], an improvement of about two orders in magnitude. The localization technique presented here enables super-resolution imaging in other physical imaging problems that use forward models, such as photoacoustic tomography [70], electrical impedance tomography [71], seismic waveform tomography [72], and microwave imaging [73]. While the experiments differ, the premise we presented should apply.

3. LOCALIZATION WITH TEMPORAL SCANNING AND MULTIGRID FOR SUPER-RESOLUTION DIFFUSE OPTICAL IMAGING[†]

We develop a model describing the measured fluorescence intensity due to multiple inhomogeneities within a highly scattering media in Section 3.1. We then use the model to localize fluorescent inhomogeneities separated in space and in time in Section 3.2, where the results are presented in Section 3.3. We use a statistical detection scheme, and we show that this method allows super-resolution diffusive optical imaging.

3.1 Models

3.1.1 Coupled Diffusion Equations

We use the diffusion approximation to the radiative transfer equation to describe the propagation of light in a highly scattering medium such as tissue [15, 75, 76]. This is an incoherent picture that has proven useful in describing the mean optical intensity when the appropriate scattering conditions are met, which is the case for tissue having millimeter thickness or more and red or near-infrared light. The coupled diffusion model in the time domain is given by [1, 44]

$$\begin{aligned} \frac{1}{v} \frac{\partial}{\partial t} \phi_x(\mathbf{r}, t) - \nabla \cdot [D_x(\mathbf{r}) \nabla \phi_x(\mathbf{r}, t)] + \mu_{a_x}(\mathbf{r}) \phi_x(\mathbf{r}, t) \\ = S_x(\mathbf{r}; t) \end{aligned} \quad (3.1)$$

$$\begin{aligned} \frac{1}{v} \frac{\partial}{\partial t} \phi_m(\mathbf{r}, t) - \nabla \cdot [D_m(\mathbf{r}) \nabla \phi_m(\mathbf{r}, t)] + \mu_{a_m}(\mathbf{r}) \phi_m(\mathbf{r}, t) \\ = \phi_x(\mathbf{r}, t) * S_f(\mathbf{r}; t), \end{aligned} \quad (3.2)$$

[†] This work is published as B. Z. Bentz, D. Lin, J. A. Patel, K. J. Webb, “Multiresolution Localization with Temporal Scanning for Super-Resolution Diffuse Optical Imaging of Fluorescence,” *IEEE Trans. Image Process.*, vol. 29, p. 830, 2019 (Ref. [74])

where \mathbf{r} denotes the position, ϕ (W/mm²) is the photon flux density, μ_a (mm⁻¹) is the absorption coefficient, $D = 1/[3(\mu_a + \mu'_s)]$ (mm) is the diffusion coefficient, $\mu'_s = \mu_s(1 - g)$ (mm⁻¹) is the reduced scattering coefficient, μ_s is the scattering coefficient (mm⁻¹), g is the anisotropy parameter, $v = c/n$ is the speed of light in the medium, where c is the speed of light in free space and n is the refractive index, the subscripts x and m , respectively, denote parameters at the excitation and emission wavelengths, λ_x and λ_m , S_x (W/mm³) is the excitation source term, S_f (s⁻¹/mm) is the fluorescence source term, and $*$ signifies a temporal convolution. The spatially-dependent fluorescence source in (3.2), assuming a single lifetime at each point in space, can be written as

$$S_f(\mathbf{r}; t) = \frac{\eta(\mathbf{r})}{\tau_f(\mathbf{r})} \exp\left(\frac{-t}{\tau_f(\mathbf{r})}\right), \quad (3.3)$$

where $\eta = \eta_f \mu_{a_f}$ is the fluorescent yield, with μ_{a_f} the fluorophore absorption coefficient at λ_x and η_f the fluorophore quantum yield, and τ_f is the fluorescence lifetime. With a temporal Fourier transform, resulting in the frequency domain form of (3.1) and (3.2), and considering homogeneous D and μ_a , the resulting scalar wave equations for ϕ describe the propagation of diffuse photon density waves (DPDW's). We present results in terms of the mean free path, $l^* = 3D$. However, the results can be scaled to geometries of different size and amount of scatter.

3.1.2 Forward Model for a Single Fluorescent Inhomogeneity

Equations (3.1) and (3.2) can be used to form a model of the detected power at λ_x and λ_m , respectively, at a set of locations around the periphery of the scattering medium. We consider the case of a set of point-emitting fluorophores, each with a differing temporal response due to the physical situation, so that the response can be attributed to a sequence of single point fluorophores. We start by describing the response due to a single fluorescent source embedded in a highly scattering medium.

The problem geometry is shown in Fig. 3.1. The incident laser light at wavelength λ_x can be modeled as an (isotropically emitting) point source for S_x in (3.1) located

l^* into the scattering medium (the brain). Point excitation sources represent a set of laser beam excitation locations at known positions \mathbf{r}_s . We therefore assume the excitation source term is given by $S_x(\mathbf{r}; t) = S_o\delta(\mathbf{r} - \mathbf{r}_s, t)$, where S_o is the excitation power (W/mm³) and $\delta(\cdot)$ is the Dirac delta. The implication is that the temporal excitation laser source is short relative to the other time constants involved. In this work, we let $S_o = 1$ for simplicity. Additionally, point detectors that collect light at λ_m are assumed to be placed at known positions \mathbf{r}_d . Finally, a fluorescent emitter (at λ_m) that is excited at λ_x is assumed to be located at the unknown position \mathbf{r}' . Using the domain geometry in Fig. 3.1, we define $g_x(\mathbf{r}_s, \mathbf{r}', t)$ as the Green's function from (3.1) at λ_x and $g_m(\mathbf{r}', \mathbf{r}_d, t)$ as the Green's function from (3.2) at λ_m . The fluorescence emission photon flux density at the detector is then

$$\begin{aligned} \phi_m(\mathbf{r}_s, \mathbf{r}_d, t) = \\ \int g_m(\mathbf{r}', \mathbf{r}_d, t) * S_f(\mathbf{r}'; t) * g_x(\mathbf{r}_s, \mathbf{r}', t) d\mathbf{r}', \end{aligned} \quad (3.4)$$

where $*$ is the temporal convolution.

We assume a point fluorophore is located at \mathbf{r}_f , as seen in Fig. 3.1, and from (3.3),

$$S_f(\mathbf{r}; t) = \frac{\eta_f \mu_{af}}{\tau_f} \exp\left(\frac{-t}{\tau_f}\right) \delta(\mathbf{r} - \mathbf{r}_f). \quad (3.5)$$

For simplicity, we assume that D and μ_a are homogeneous, and that v is the same at λ_x and λ_m . Using the Green's function solution to the diffusion equation [1], we find from (3.4) that

$$\begin{aligned} \phi_m(\mathbf{r}_s, \mathbf{r}_f, \mathbf{r}_d, t) = \\ \frac{v}{(4\pi D_m vt)^{3/2}} \exp\left(\frac{-|\mathbf{r}_d - \mathbf{r}_f|^2}{4D_m vt} - \mu_{am} vt\right) \\ * \frac{\eta}{\tau_f} \exp\left(\frac{-t}{\tau_f}\right) \\ * \frac{v}{(4\pi D_x vt)^{3/2}} \exp\left(\frac{-|\mathbf{r}_f - \mathbf{r}_s|^2}{4D_x vt} - \mu_{ax} vt\right). \end{aligned} \quad (3.6)$$

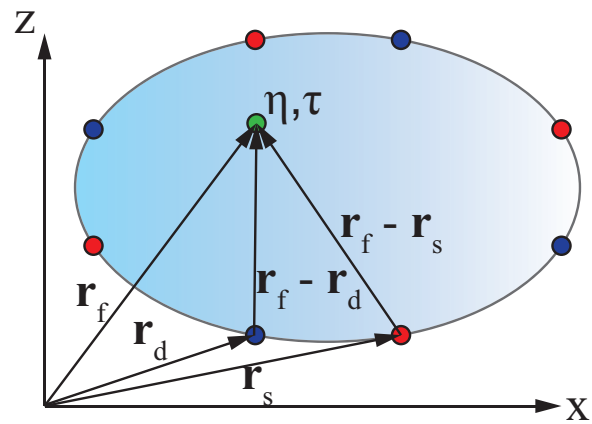


Fig. 3.1. Model geometry with position vector $\mathbf{r} = (x, z)$. Excitation sources at λ_x (red) are placed at known positions \mathbf{r}_s , point fluorescence emission locations are assumed to be \mathbf{r}_f (green), and detectors at λ_m are placed at known positions \mathbf{r}_d (blue).

We also assume that $\mu_{a_x} = \mu_{a_m} = \mu_a$ and $D_x = D_m = D$. The detected power through an aperture is described by the current density \mathbf{J} (W/mm²), with a diffusion framework, and we assume pointwise measurements

$$\mathbf{J}(\mathbf{r}_s, \mathbf{r}_f, \mathbf{r}_d, t) = -D\nabla\phi_m(\mathbf{r}_s, \mathbf{r}_f, \mathbf{r}_d, t). \quad (3.7)$$

For laser excitation source locations \mathbf{r}_{s_q} with $q \in [1, \dots, Q]$ and fluorescence detector locations \mathbf{r}_{d_m} with $m \in [1, \dots, M]$, we write the detected fluorescent photon current density in compact form as

$$\mathbf{J}_{qm}(\mathbf{r}_f, t) = \mathbf{J}(\mathbf{r}_{s_q}, \mathbf{r}_f, \mathbf{r}_{d_m}, t), \quad (3.8)$$

where we emphasize the dependence on \mathbf{r}_f because it will be estimated in Section 3.2. The pointwise detected fluorescence is then

$$G_{qm}(\mathbf{r}_f, t) = |\mathbf{J}_{qm}(\mathbf{r}_f, t) \cdot \hat{\mathbf{n}}|, \quad (3.9)$$

where $\hat{\mathbf{n}}$ is the unit vector normal to the detector surface and G signifies the (diffusion equation) Green's function basis.

For simplicity we use the analytic solution (3.9) in this work, but the model data could also be generated using finite element or other numerical methods [53]. These analytical solutions to the diffusion equation subject to boundary conditions have been shown to match experiments of photon propagation in highly scattering media [21, 54]. It has been shown that small fluorescent inhomogeneities can be well approximated as point emitters because of the rapid attenuation of high spatial frequencies in scattering media [21, 55]. For this reason, imaging based on a point representation is possible.

3.1.3 Forward Model for Multiple Fluorescent Inhomogeneities

In the case where multiple fluorescent inhomogeneities are present, the forward model must be modified. We assume each fluorescent inhomogeneity can be represented by a point that fluoresces with a unique and increasing delay τ from $t = 0$. We

let K fluorescent inhomogeneities be located at positions \mathbf{r}_{f_k} , where k is an index from 1 to K . Each fluorescent inhomogeneity has a different yield η_k and fires with different delay τ_k from $t = 0$. Then, the detected fluorescence for a single source-detector pair measured over the temporal support w starting at time t_o is

$$\tilde{G}_{qm}(\mathbf{R}, \boldsymbol{\tau}, t) = \text{rect}\left(\frac{t - 0.5w - t_o}{w}\right) \times \sum_{k=1}^K \delta(t - \tau_k) * G_{qm}(\mathbf{r}_{f_k}, t), \quad (3.10)$$

where for general x , $\text{rect}(x)$ is 1 when $|x| < 0.5$ and zero otherwise, the vector $\boldsymbol{\tau} = [\tau_1 \dots, \tau_K]^T$ corresponds to the delays τ_k , and the vector \mathbf{R} contains the K positions \mathbf{r}_{f_k} .

We assume the detected fluorescence from (3.10) is sampled with sampling interval T , and we discretize the domain such that V_{vox} is the volume of a single voxel, giving the forward measurements

$$f_{qmn}(\mathbf{R}, \boldsymbol{\tau}) = V_{vox} \left[\tilde{G}_{qm}(\mathbf{R}, \boldsymbol{\tau}, t)|_{t=nT} \right] \quad (3.11)$$

where n is an index from 1 to N , and $t_{max} = NT$. We emphasize the dependence on \mathbf{R} and $\boldsymbol{\tau}$ because these parameters will be estimated in Section 3.2. We can now write the fluorescence data vector expected from the diffusion model as $\mathbf{f}(\mathbf{R}, \boldsymbol{\tau})$, which is

$$\mathbf{f}(\mathbf{R}, \boldsymbol{\tau}) = [f_{111}, \dots, f_{11N}, f_{121}, \dots, f_{12N}, \dots, f_{1M1}, \dots, f_{1MN}, f_{211}, \dots, f_{QMN}]^T. \quad (3.12)$$

Considering (3.6), each \tilde{f}_{qm} is linear with respect to η_k such that we can pull out the η_k 's from $\mathbf{f}(\mathbf{R}, \boldsymbol{\tau})$, giving

$$\mathbf{f}(\mathbf{R}, \boldsymbol{\tau}) = \mathbf{F}(\mathbf{R}, \boldsymbol{\tau})\boldsymbol{\eta}, \quad (3.13)$$

where $\boldsymbol{\eta} = [\eta_1 \dots, \eta_K]^T$ is a vector containing the fluorescent yields η_k and $\mathbf{F}(\mathbf{R}, \boldsymbol{\tau})$ is a matrix of dimensions $[QMN, K]$ that contains the scaled forward measurements. The matrix $\mathbf{F}(\mathbf{R}, \boldsymbol{\tau})$ can be calculated from (3.10) by setting all η_k equal to 1. The vector multiplication in (3.13) is equivalent to the superposition of the K fluorescent inhomogeneity temporal responses, which, after scaling, make up the columns of $\mathbf{F}(\mathbf{R}, \boldsymbol{\tau})$.

3.1.4 Detector Noise

We use a shot noise model for detector noise [11, 57]. We let \mathbf{y} be the noisy measurement vector corresponding to \mathbf{f} , such that both have dimensions of $[QMN, 1]$. We assume that the noise is independent, zero mean, and Gaussian with covariance Υ , where

$$[\Upsilon]_{ii} = \alpha |y_i|, \quad (3.14)$$

$i = [1, \dots, QMN]$ is the data index, and α is a scalar parameter that is dependent on the noise detector physics [11]. The SNR in dB for a single source-detector pair depends on α according to

$$\text{SNR} = 10 \log \left[\frac{1}{\alpha} f_{qmn}(\mathbf{R}, \boldsymbol{\tau}) \right]. \quad (3.15)$$

We generate simulated noisy measurements \mathbf{y} for a specified SNR by calculating α from (3.15).

3.2 Localization for Super-Resolution Imaging

Compared to diffusive imaging with FDOT, fluorescence localization is a simpler problem where information about an inhomogeneity's location is extracted [19–21, 77, 78]. Biomedical applications of localization include determining the location of a fluorescing tumor in a mouse [23] or the location of a targeted fluorophore embedded in the tongue of a live mouse [79]. Here, we describe localization of multiple fluorescent inhomogeneities for the formation of super-resolution images. Our method assumes there is a significant temporal separation τ_f such that the fluorescent impulse responses can be separated. By exploiting this information as prior knowledge, higher resolution imaging compared to FDOT is achieved.

3.2.1 Localization of Multiple Fluorescent Inhomogeneities

In order to localize K fluorescent inhomogeneities inside a highly scattering medium, the positions \mathbf{r}_{f_k} must be estimated. To further characterize the fluorescent inhom-

genities, the yields η_k , which are proportional to the concentration of fluorophore, can also be estimated. We form the ML estimation as [21, 55]

$$\hat{\theta} = \arg \max_{\theta} p_{1,\theta}(\mathbf{y}), \quad (3.16)$$

where $p_{1,\theta}(\mathbf{y})$ is the probability distribution given by

$$p_{1,\theta}(\mathbf{y}) = \frac{1}{\sqrt{(2\pi)^P |\mathbf{\Upsilon}|}} \exp\left(-\frac{1}{2} \|\mathbf{y} - \mathbf{F}(\mathbf{R}, \boldsymbol{\tau})\boldsymbol{\eta}\|_{\mathbf{\Upsilon}^{-1}}^2\right), \quad (3.17)$$

where $P = QMN$ is the number of measurements, for an arbitrary vector \mathbf{u} , $\|\mathbf{u}\|_{\mathbf{V}}^2 = \mathbf{u}^H \mathbf{V} \mathbf{u}$, H being the Hermitian transpose, and θ corresponds to the parameters of interest for localization, which are \mathbf{R} and $\boldsymbol{\eta}$. After taking the logarithm, (3.16) is equivalent to minimizing

$$c(\mathbf{R}, \boldsymbol{\tau}) = \min_{\boldsymbol{\eta}} \|\mathbf{y} - \mathbf{F}(\mathbf{R}, \boldsymbol{\tau})\boldsymbol{\eta}\|_{\mathbf{\Upsilon}^{-1}}^2. \quad (3.18)$$

We propose a method to minimize (3.18) that takes advantage of the causality of the problem. This approach allows us to avoid calculation of the basis functions at each τ_k and their inner products, alleviating the computation burden. We assume that each τ_k is unique, allowing temporal separation of the fluorescent impulse responses, as shown in Fig. 3.2 for the case of two emitters. In Fig. 3.2(a) the temporal responses from two point fluorophore locations in a scattering domain are measured to be displaced in time but overlapping, whereas in Fig. 3.2(b) they are distinct. We consider the general case where the delays τ_k are not large enough for the fluorescence to decay to noise before the start of the next response, as shown in Fig. 3.2(a). The discretized measurement data leads to a temporal sampling period T and we consider a temporal window w , illustrated in Fig. 3.2, consisting of an integer number of samples separated in time by T .

Considering (3.10), we see that η_k and \mathbf{r}_{f_k} could be estimated using data within a temporal window starting at $t_o = \tau_k$ with $w < \tau_{k+1} - \tau_k$. Thus, we assume that the data within the temporal window w comes from a single fluorophore at \mathbf{r}_{f_k} . A simplified cost function based on (3.18) can then be written as

$$c_k(\mathbf{r}_{f_k}, \tau_k) = \min_{\eta_k} \|\mathbf{y}_k - \eta_k \mathbf{f}_k(\mathbf{r}_{f_k})\|_{\mathbf{\Upsilon}_k^{-1}}^2, \quad (3.19)$$

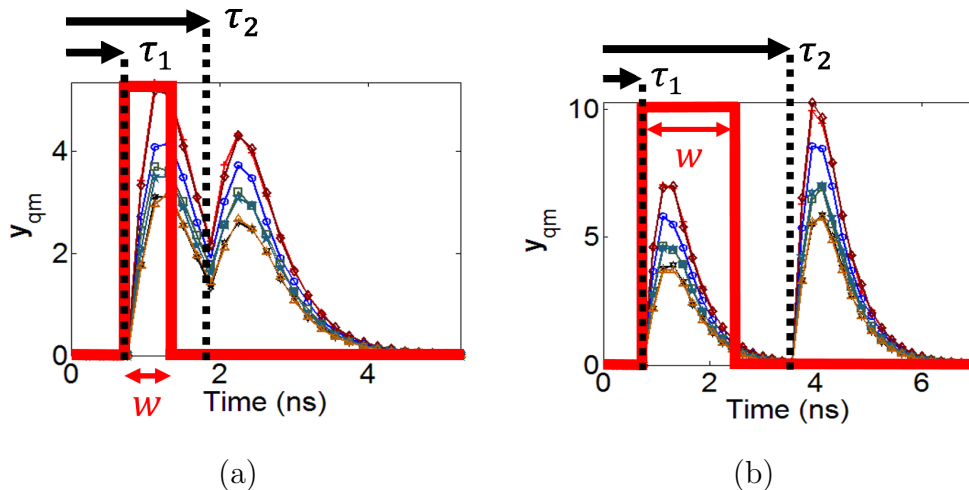


Fig. 3.2. Typical fluorescence temporal responses for one source and seven detectors ($Q = 1$, $M = 7$). The optical properties are similar to tissue, where $\mu'_s = 2 \text{ mm}^{-1}$, $\mu_a = 0.02 \text{ mm}^{-1}$, and $n = 1.33$, giving a mean free path length $l^* = 3D = 0.5 \text{ mm}$. The 7 different symbols and corresponding colors represent different source-detector measurement pairs. The time axis is a discrete set of points t_1, \dots, t_N , with T between sample points. (a) The delay τ_2 is short, causing substantial overlap due to superposition. (b) The delay τ_2 is long such that the detected fluorescence decays substantially before the next fluorescence response. We show that localization of the fluorescence inhomogeneities is possible in both cases.

where $\mathbf{f}_k(\mathbf{r}_{f_k})$ is derived from $\mathbf{f}(\mathbf{R}, \boldsymbol{\tau})$ in (3.12) with $t_o = \tau_k$ and $w < \tau_{k+1} - \tau_k$, \mathbf{y}_k is the corresponding windowed measurement vector, and $\boldsymbol{\Upsilon}_k$ is the noise covariance matrix for \mathbf{y}_k . In this description, \mathbf{y}_k contains the subset of measurements from \mathbf{y} at all detectors that are within w . Note that w is being used here as a model parameter to identify the response of a single point fluorophore, and that the measured data \mathbf{y} has a temporal support that is much larger than w .

Forming (3.19) requires that τ_k is known. We estimate τ_k using the generalized likelihood ratio test (GLRT) [21]. The GLRT uses a binary hypothesis to calculate a threshold for determining whether a point fluorophore is detectable or “localizable”. We apply the GLRT at each time index starting at $t = 0$ and progressing in positive time in increments of T . The time index where a fluorescent inhomogeneity is first detected is then our estimate for τ_k . Once detectability is established, (3.19) can be minimized using the estimated τ_k and a preselected w . To detect the next emitter, in general the estimated forward solution $\hat{\mathbf{y}}_k = \hat{\eta}_k \mathbf{f}(\hat{\mathbf{r}}_{f_k})$, must be subtracted from \mathbf{y} before before moving the temporal window w and calculating the GLRT at the next time point. This removes the influence of one reporter’s response from the responses following it, and is valid by superposition. The robustness of the method can be improved by adding positive noise to $\hat{\mathbf{y}}_k$ before subtraction, where values that are negative after subtraction are set to zero.

We also consider the special case where w can be large compared to the decay time of the fluorescence responses. This is shown in Fig. 3.2(b), demonstrating that the subtraction step is not needed if the time scan is resumed at $t = \tau_k + w$. However, we use the general case which allows extraction of the response of each fluorescent inhomogeneity from the signals in Fig. 3.2(a) or (b).

To minimize (3.19), we use the method developed by Milstein *et al.* [21], which is a two step procedure described by

$$\tilde{\eta}_k(\mathbf{r}_{f_k}) = \frac{\mathbf{f}_k^T(\mathbf{r}_{f_k}) \boldsymbol{\Upsilon}_k^{-1} \mathbf{y}_k}{\mathbf{f}_k^T(\mathbf{r}_{f_k}) \boldsymbol{\Upsilon}_k^{-1} \mathbf{f}_k(\mathbf{r}_{f_k})} \quad (3.20)$$

$$c_k(\mathbf{r}_{f_k}, \tau_k) = \|\mathbf{y}_k - \tilde{\eta}_k(\mathbf{r}_{f_k}) \mathbf{f}_k(\mathbf{r}_{f_k})\|_{\boldsymbol{\Upsilon}_k^{-1}}^2. \quad (3.21)$$

Equation (3.20) was found by setting the derivative of $\|\mathbf{y}_k - \eta_k \mathbf{f}_k(\mathbf{r}_k)\|_{\mathbf{r}_k}^2$ with respect to η_k equal to zero. Equations (3.20) and (3.21) are then solved at positions \mathbf{r}_{f_k} of interest (within the time window w), and the k th fluorescent inhomogeneities' position and yield are estimated by

$$\hat{\mathbf{r}}_{f_k} = \arg \min_{\mathbf{r}_{f_k}} c_k(\mathbf{r}_{f_k}, \tau_k) \quad (3.22)$$

$$\hat{\eta}_k = \tilde{\eta}_k(\hat{\mathbf{r}}_{f_k}). \quad (3.23)$$

In an experiment, where calibration scale factors are unknown, $\hat{\eta}_k$ can be considered a nuisance parameter [21] where its estimate is no longer quantitative.

We demonstrate localization of a single fluorescent inhomogeneity using optical properties similar to tissue in Fig. 3.3. For simplicity, we assume a two dimensional geometry and a region of interest of length $32 \times l^*$ along x and of length $32 \times l^*$ along z , where the mean free path length $l^* = 3D$. Extension to three dimensions is unnecessary to demonstrate the method, but it is straightforward. We place a single source and seven detectors along the boundary of the region of interest, as seen in Fig. 3.3. We use a discretized grid with $N_x = 64$ points in the x dimension and $N_z = 64$ points in the z dimension. The position with lowest cost in Fig. 3.3(b) is $\hat{\mathbf{r}}_f$, and the value of $\tilde{\eta}_k$ at $\hat{\mathbf{r}}_{f_k}$ in Fig. 3.3(a) is $\hat{\eta}_k$. Here, $\hat{\mathbf{r}}_{f_k} = (x, z) = (15.24, 15.75) \times l^*$ and $\hat{\eta} = 0.0999 \text{ mm}^{-1}$, which are close to the true values given in the Fig. 3.3 caption. We calculated the localization error as $[(\mathbf{r}_{f_k} - \hat{\mathbf{r}}_{f_k})/\mathbf{r}_{f_k} \times 100]\%$. The results can be extrapolated to three dimensions, and the problem is scalable in the amount of scatter.

3.2.2 Localization with Multigrid

We introduce a method to simultaneously reduce the computation time and improve the accuracy of the localization by incorporating a hierarchy of discretization grids into the localization. We refer to this as a multiresolution analysis (MRA) method [56, 57], and it is demonstrated in Fig. 3.4. First, $c_k(\mathbf{r}_{f_k}, \tau_k)$ is calculated using (3.20) and (3.21) on a coarse grid over the entire region of interest. Then,

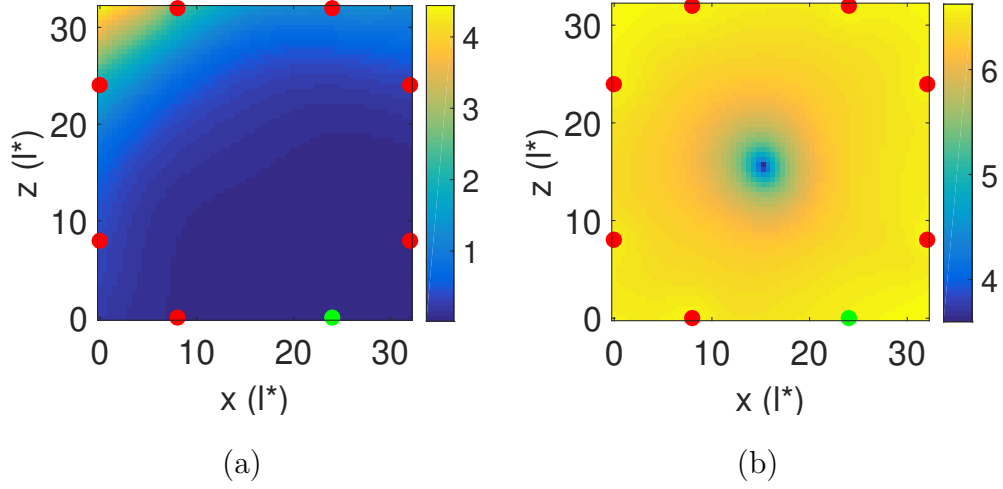


Fig. 3.3. Localization of a single fluorescent inhomogeneity ($K = 1$) using an (x, z) coordinate system. 1 source (green) and 7 detectors (red) are placed at the boundary of a square of side length $32l^*$. The optical properties are the same as in Fig. 3.2, where $l^* = 0.5$ mm, and we assume an SNR of 30 dB. A fluorescent inhomogeneity with $\eta_1 = 0.1$ mm⁻¹ was placed at $x = 15.26 \times l^*$ and $z = 15.56 \times l^*$. The simulated noisy data is the same as the first set of curves at τ_1 shown in Fig. 3.2(b). (a) Yield $\tilde{\eta}_k(\mathbf{r}_{f_k})$ from (3.20) plotted over the region of interest. (b) Cost $c_k(\mathbf{r}_{f_k}, \tau_k)$ from (3.21) plotted over the region of interest. The position with lowest cost in (b) is $\hat{\mathbf{r}}_{f_k}$, and the value of $\tilde{\eta}_k$ at $\hat{\mathbf{r}}_{f_k}$ in (a) is $\hat{\eta}_k$. Here, $\hat{\mathbf{r}}_{f_k} = (x, z) = (15.24, 15.75) \times l^*$ and $\hat{\eta}_k = 0.0999$ mm⁻¹. The percent errors in the estimated x and z positions are 0.143% and 1.196%, respectively. The discretization of the region of interest is a primary contributor to the estimation error.

$c_k(\mathbf{r}_{f_k}, \tau_k)$ is iteratively calculated on successively finer and finer grids, such that each new grid contains the point of minimum cost. This procedure is repeated until convergence, which, in our case, was two grids where the change in the minimum cost was less than 1%, but not equal to 0. Importantly, not converging when the change in cost is zero avoids the situation where the same point happens to have the lowest cost on two grids.

3.3 Results

We show localization of four different fluorescent inhomogeneities separated by varying delays. We use the same geometry and optical parameters as in Fig. 3.3, except we place four inhomogeneities within the medium instead of one.

Figure 3.5 (a) plots the problem geometry as in Fig. 3.3, where the positions of the excitation source (green), detectors (red), and fluorescent inhomogeneities (cyan) are shown. Figure 3.5 (b) shows the simulated noisy data from the four inhomogeneities with delays of 0.9, 3.75, 7.5, and 8.6 ns. The first two inhomogeneities are temporally separated, while the second two have a significant temporal overlap. Figure 3.5 (c) plots the actual and predicted locations of the inhomogeneities, which are separated by $0.2 \times l^*$. Fig. 3.5 (d) shows the yield η (proportional to concentration) experimental errors, calculated as $[(\eta_k - \hat{\eta}_k)/\eta_k \times 100]$. For the multigrid operation, we used $N_x = N_z = 5$ equally spaced points for each grid, the same as what was used in Fig. 3.4. The first coarse grid was defined over the entire square region of interest from Fig. 3.3, and each finer square grid was centered at (3.22) and extended a distance slightly greater than the previous grid spacing along the x and z directions (similar to Fig. 3.4). Both the position and η were predicted with high accuracy, even for the case when there is overlap between the temporal signals. The accuracy of the localization is the focus of Section 3.3.1.

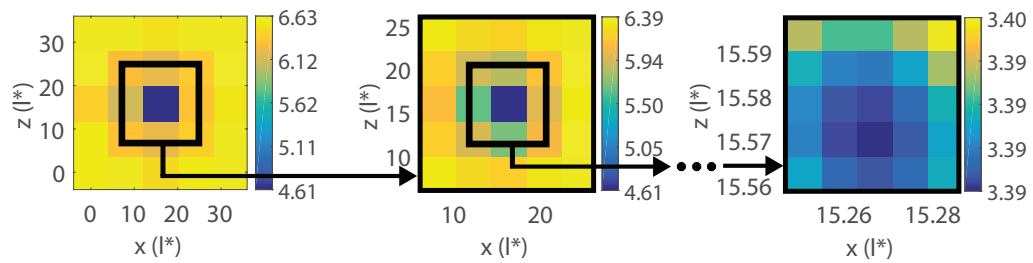


Fig. 3.4. Localization with MRA of the single fluorescent inhomogeneity in Fig. 3.3. The cost is calculated using (3.20) and (3.21) on progressively finer grids, where each new grid contains the region of smallest cost. Here, $\hat{\mathbf{r}}_{f_k} = (x, z) = (15.27, 15.57) \times l^*$ and $\hat{\eta}_k = 0.1003 \text{ mm}^{-1}$. The percent errors in the estimated x and z positions are 0.037% and 0.066%, respectively. The discretization error has been reduced, especially for the z coordinate. The number of positions where the cost must be calculated has also been reduced, decreasing the computation time. The reduction is even greater when extrapolated to 3D.

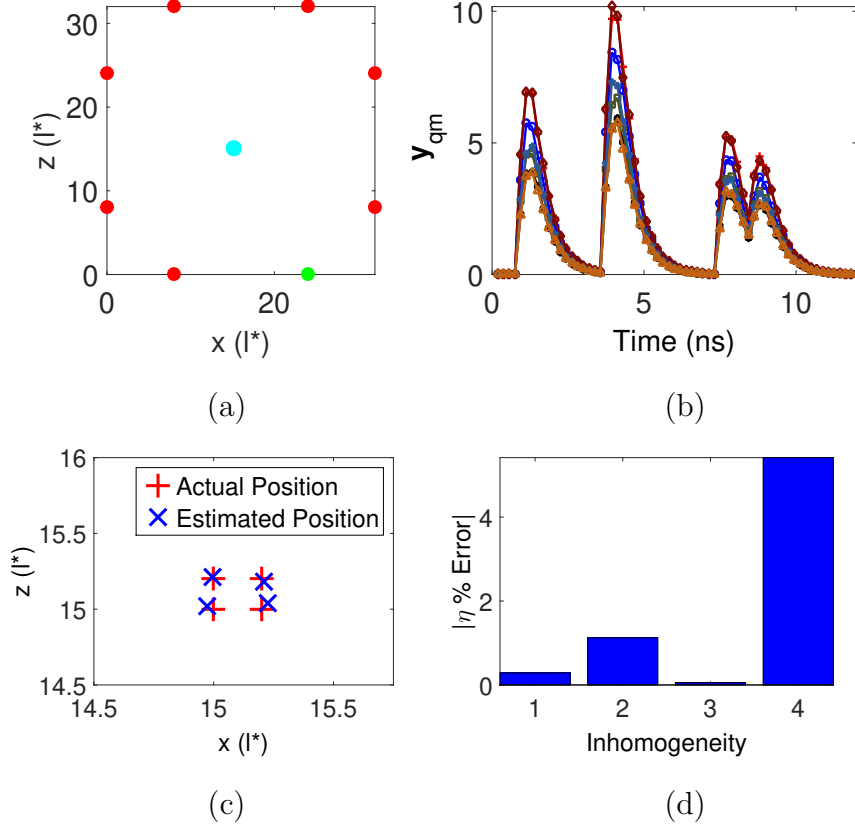


Fig. 3.5. Localization of four fluorescent inhomogeneities at different positions with different delays and yields using the same optical parameters as in Fig. 3.2 and the same geometry as in Fig. 3.3. The true parameters describing the inhomogeneities are $(x, z, \eta, \tau) = (15l^*, 15l^*, 0.1, 5T)$, $(15l^*, 15.2l^*, 0.15, 20T)$, $(15.2l^*, 15.0l^*, 0.075, 40T)$, and $(15.2l^*, 15.2l^*, 0.05, 46T)$, where $l^* = 0.5$ mm and $T = 0.19$ ns. All of these parameters are estimated by the algorithm. We assume the fluorescence lifetime τ_f is known. (a) Problem geometry as in Fig. 3.3, where the positions of the excitation source (green), detectors (red), and fluorescent inhomogeneities (cyan) are plotted. (b) Detected fluorescence temporal profile. One source ($Q = 1$) and seven detectors ($M = 7$) give 7 measurements \mathbf{y}_{qm} . The 7 different symbols and their corresponding colors represent different source-detector measurement pairs. The data was generated using the true parameters with 30dB of simulated noise. (c) True positions of the inhomogeneities \mathbf{r}_k and the estimated positions $\hat{\mathbf{r}}_{f_k}$ determined by the localization algorithm. Note the accuracy of the estimated positions. (d) Yield η_k experimental errors. Labels one to four correspond to delays from shortest to longest. Each fluorescent inhomogeneity was successfully localized, even for the case when there is overlap between the temporal signals.

3.3.1 Localization for High Spatial Resolution

We assume insignificant background signal and that the fluorophores do not diffuse or change positions significantly during the integration time. In this case, each $\hat{\mathbf{r}}_{k_f}$ coordinate x and z has a Gaussian probability distribution characterized by the standard deviations σ_x and σ_z . These standard deviations are commonly used to characterize the spatial precision of localization [60, 62]. Here, we show the capability of localization to extract high-spatial-resolution information by generating these statistics from numerical calculations.

We iteratively localize the single inhomogeneity in Fig. 3.3 using MRA, and the results are shown in Fig. 3.6. During each iteration, random noise was added to the forward calculation in order to generate independent simulated measurements. σ_x and σ_z were then calculated from the localized positions and used to plot ellipses with major and minor axis equal to $4\sigma_x$ or $4\sigma_z$. The MRA method described in Section 3.2.2 is essential to reducing the time required to compute these statistics.

Figure 3.6(a) and (b) show localization uncertainty statistics for different SNR, where the noise was added as described by (3.14) [11]. Even for a low SNR of 10 dB, the location of the fluorescent inhomogeneity can be estimated with much higher accuracy compared to traditional diffusive imaging methods. Figure 3.6(c) and (d) show localization uncertainty statistics for different numbers of detectors M . The detectors were distributed as in Fig. 3.3, and the statistics depend on the spatial support. Compared to volumetric image reconstruction with FDOT, little information, or fewer detectors, are needed to localize the fluorescent inhomogeneity.

To study how the localization uncertainty will depend on the window length w , we build up localization uncertainty statistics for different w with a constant SNR of 30 dB and $M = 7$. The results are shown in Fig. 3.6(e) and (f). For all results in this figure (and also in Fig. 3.5), the time axis starts at $t = 0$ and continues in increments of $T = 0.19$ ns for 64 increments, giving $t_{max} = 12.16$ ns. As can be seen in Fig. 3.6(e)

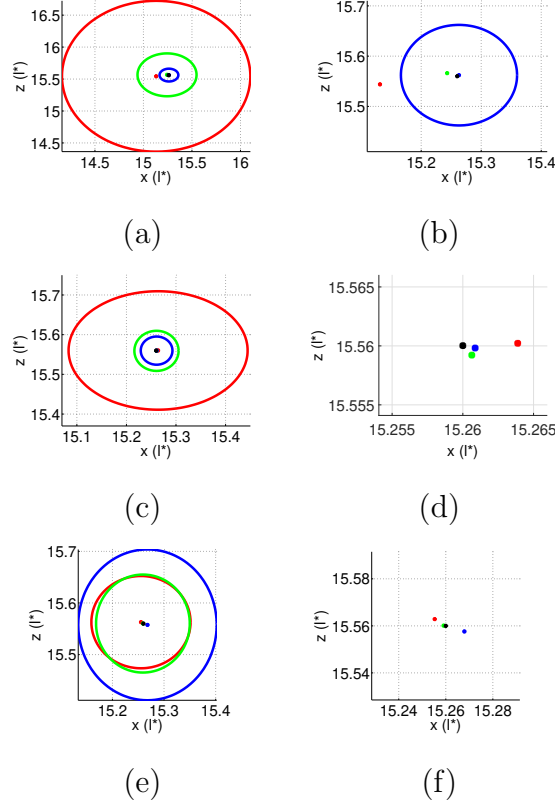


Fig. 3.6. Localization uncertainty of a single fluorescent inhomogeneity using the same optical parameters as in Fig. 3.2 and the same geometry as in Fig. 3.3 with $Q = 1$. The fluorescent inhomogeneity location was estimated 150 times using noisy simulated independent data sets. The true location is the black point. The ellipses have major and minor axes of length $4\sigma_x$ or $4\sigma_z$, such that they contain 95% of the \hat{x} and \hat{z} positions. The center points of the ellipses are the mean of the \hat{x} and \hat{z} positions. (a) Localization uncertainty for different SNR with $M = 7$ and $w = 3T$. Blue, green, and red correspond to SNR of 30, 20, and 10 dB, respectively. (b) Zoomed version of (a) to show the mean values. (c) Localization uncertainty for different numbers of detectors M with 30 dB noise and $w = 3T$. Red, green, and blue correspond to $M = 7$, $M = 31$, and $M = 50$. (d) Enlarged version of (c) to show the mean values. (e) Localization uncertainty for different window lengths w , 30 dB SNR, and $M = 7$. Red, green, and blue correspond to windows $w = 32T$, $17T$, and $2T$, where $T = 0.19$ ns and $t_{max} = 64T$. (f) Enlarged version of (e) to show the mean values. The ellipses are not circles because the fluorescent inhomogeneity is not located at the center of the medium and equidistant to all detectors. Note that the fluorescent inhomogeneity can be accurately localized even with low SNR, few detectors, and a short window w .

and (f), the localization statistics change slightly with window size, but they are still highly accurate even for the shortest window of length $2T$.

The localization uncertainty of the inhomogeneities in Fig. 3.5(c) is described by the blue ellipse in Fig. 3.6(b). The extension to imaging is straightforward. If we consider an image which is made up of voxels, and each voxel can be individually localized, then Fig. 3.6 describes the resolution limit of the image, the minimum distance between two inhomogeneities such that they can both be accurately localized, is about $0.1l^*$ or $50 \mu\text{m}$. This is a remarkable spatial resolution for deep tissue optical imaging.

3.4 Discussion

We have shown that localization is a powerful tool for retrieving high spatial and temporal resolution information of fluorescent inhomogeneities embedded in scattering media. To accomplish this, we have assumed as prior information that the data from each fluorescent inhomogeneity is separated by a varying and increasing delay. Interestingly, because the scattering medium acts as a low pass spatial frequency filter [33], the method is relatively robust to noise. Our incorporation of a forward model, such as the coupled diffusion model for scattered light we use here, allows imaging through scatter. Moreover, our super-resolution imaging method can be applied to a wider variety of applications that employ forward models, such as photoacoustic tomography [80], seismic waveform tomography [81], and microwave imaging [82].

One important potential application is brain imaging, because the response of fluorescent contrast agents due to neurons or groups of neurons firing may follow a model similar to in (3.10) [83–87]. If this is found to be true, and a reasonable SNR can be achieved, then it would be possible to form images of the whole brain or brain surface with high spatial and temporal resolution. These images could be used to form correlation maps of brain activity, useful for diagnosing and studying neurological diseases such as Parkinson’s or Alzheimer’s disease, and developing treatments [88].

Considering Fig. 3.3, only one source and a few detectors are required, simplifying the experiment setup. The experiment could be performed in the time domain with fast and sensitive detectors, or with an integration time equal to w if the delays τ_k are sufficiently large. Data captured with an intensified CCD over an integration time of w could be used to separate temporally overlapping neuron responses in time and in space due to the large number of detectors. Another potential application is the localization of blinking quantum dots [68].

Outside of fluorescence imaging altogether, our method may be applied to, for example, acoustic waves generated by multiple speakers in a room. A suitable forward model can easily be obtained if the shape of the room is known in advance, and the required intermittent generation of sound may arise in normal conversation between people. Our method could then be used to localize these speakers, and once that is achieved, we envision the location-specific amplification or attenuation of certain speakers, thus allowing a measure of control over the acoustic environment.

3.5 Conclusion

We have developed an approach for fast localization of multiple fluorescent inhomogeneities within a highly scattering medium that takes advantage of variations in temporal delays between responses. The method allows formation of super-resolution optical images from highly scattered light. We demonstrate through simulations that MRA and temporal scanning can significantly reduce the computational burden. The geometries can be scaled and other forward models can be used, allowing a broad range of applications.

4. MOTION IN STRUCTURED ILLUMINATION

Controlled nanometer-scale movement of an object in a spatially varying field provides far-subwavelength information and a new sensing and imaging modality. Considering the one-dimensional case, where a film is moved in a standing wave, we show that measured power data as a function of object position provides sensitivity to the film refractive index and far-subwavelength thickness. Use of a cost function allows iterative retrieval of the film parameters, and a multi-resolution framework is described. The approach provides an alternative to ellipsometry with additional information that circumvents the need to fit measurements to a frequency-dependent material parameter model. An instrument could use a piezoelectric positioner to move the sample, and a measurement done in transmission or reflection.

4.1 Concept

An illustration of the arrangement used to obtain simulated data is shown in Fig. 4.1. The 1D object to be characterized is located and scanned within a cavity having a low quality (Q) factor that provides the structured field. Two dielectric slabs forming the partially reflective mirrors have a refractive index of 1.5 (simulating crown glass) and a thickness of $\lambda/5$, with λ being the free-space wavelength, $1.5\mu\text{m}$. The mirrors are separated by 2.7λ (inner face-to-face distance). Note that the length of the cavity was not tuned to resonance. An object of total thickness $\lambda/5$, is comprised of two layers of different materials: a slab with a known refractive index of 1.5 and a thin film on top with a thickness L and refractive index n . Both L and n are to be determined simultaneously at the single frequency of the measurement, at λ . The numerical finite element method [89] simulations we used has a normally-incident plane wave coming in from the top, with λ and the polarization in the $\hat{\mathbf{z}}$ direction (out

of the page). Port boundary conditions were used at the top of the domain to set up the incident field while prescribing a non-reflecting condition, and periodic boundary conditions were applied to the sides. In the scattered field solution, A perfectly matched layer of thickness 0.2λ is set 0.3λ below the detector plane. In Fig. 4.1, as the object moves vertically within the structured field with subwavelength steps to a set of positions (achievable with a piezoelectric positioner), we measure the time-averaged Poynting vector magnitude, S , in the transmission direction at the detector plane, as a function of the position (Δy) of the object. In other words, when the object is scanned over K positions in the cavity, the measurement array will consist of K individual data values, each representing the measured S at each object position. For this simulation, the detector plane is located 0.4λ below the bottom surface of the lower mirror, although for the single (separable) plane wave problem considered, this distance is arbitrary. The object to be characterized is initially placed with the bottom surface 0.8λ above the top surface of the bottom mirror and scanned in small steps upwards over a range of 0.5λ , giving 21 positions and measurements in total. We assume a Gaussian noise model, such that the measurements are normally distributed with a mean equal to the noiseless measurement, S , and a standard deviation σ proportional to the noiseless data, giving us a measure of the variability of the measured signal. We choose a conservative signal-to-noise ratio (SNR) of 30 dB, which can be achievable with an appropriate input power source and integration time, for all results. The standard deviation, σ , is determined from the SNR, given by $\text{SNR}_{dB} = 10 \log_{10}(S/\sigma)$.

In Fig. 4.2(a) and (b), we plot noiseless measured data $S(\Delta y; L, n)$ with simulated noise represented as error bars against the positions of different slab configurations. In Fig. 4.2(a), the two plotted curves represent measurements of two different film refractive indices ($n = 2.00$ and $n = 1.95$) with a fixed thickness ($L = 0.005\lambda$), while Fig. 4.2(b) shows measurements of two different film thicknesses ($L = 0.007\lambda$ and $L = 0.005\lambda$) with a fixed refractive index ($n = 2.00$). In Fig. 4.2(a) and (b), we show error bars at each measured data point, where the end-to-end length of the error bars is equal to 4σ , representing the range of 95% of the noisy measurements.

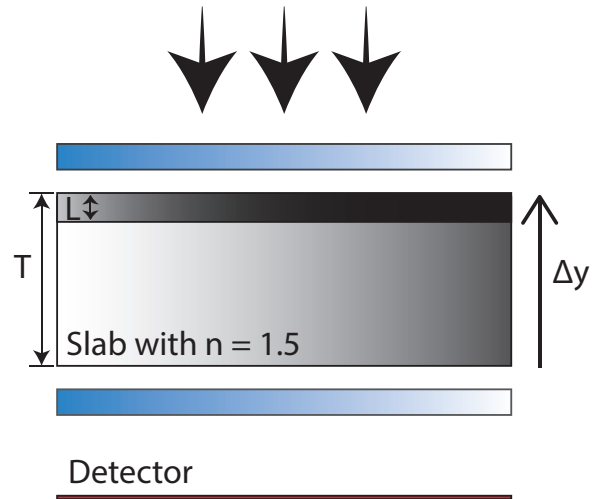


Fig. 4.1. The simulated measurement arrangement has a plane wave incident from the top, with the free-space wavelength as $\lambda = 1.5\mu\text{m}$. Two dielectric slabs act as partially reflecting mirrors and form a low- Q cavity with a length of 2.7λ (inner face-to-face distance). An object comprised of a thin film on top of a substrate, and a total thickness of $T = \lambda/5$, is located in this cavity and moved vertically upwards in nm-scale increments. As the object is translated in the cavity to a set of positions, the power is measured at the detector plane, located 0.4λ below the bottom surface of the lower mirror.

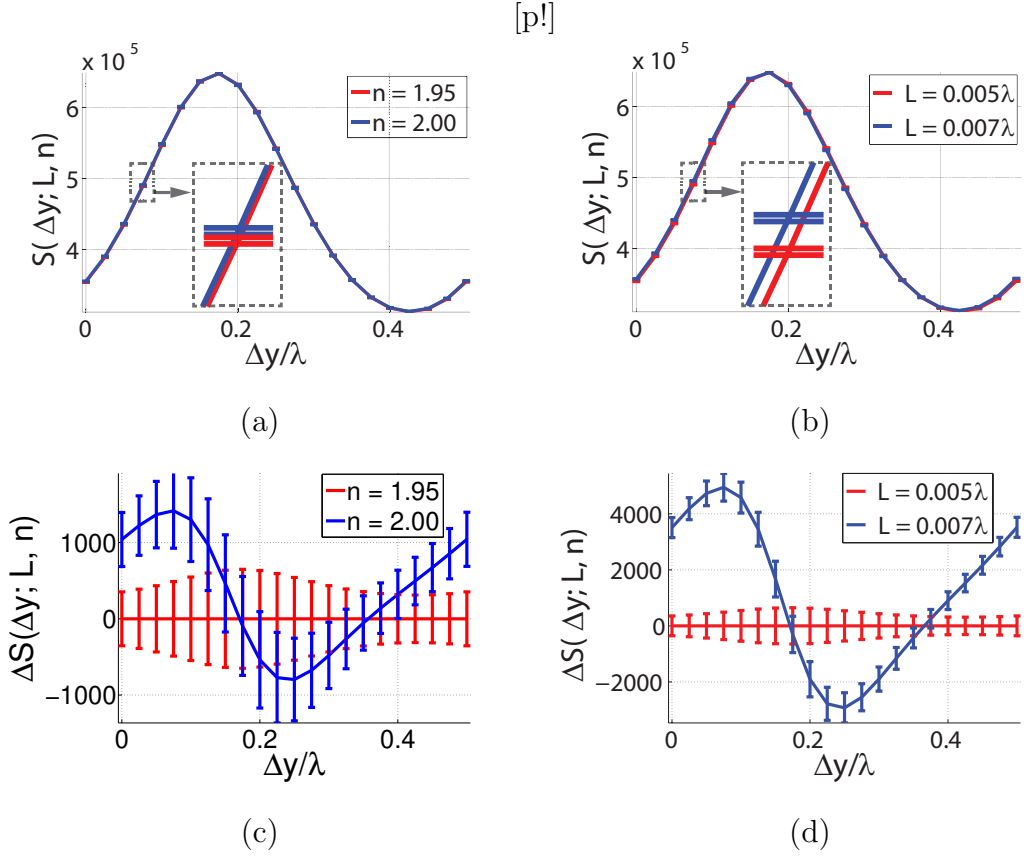


Fig. 4.2. Measured power flow against object position for different film parameters. The end-to-end length of the error bars is equal to 4σ , calculated with an SNR of 30 dB. (a) Film with $L = 0.005\lambda$ and varying refractive indices, n . (b) Film with $n = 2.00$ and different thicknesses, L . (c) Expanding the scale in (a), the red curve uses $S(\Delta y; L, 1.95)$ as a reference by setting it to zero, and the blue curve gives $[S(\Delta y; L, 2.00) - S(\Delta y; L, 1.95)]$. (d) Expanding the scale in (b), the red curve shows $S(\Delta y; 0.005\lambda, n)$ as a reference (zero), and the blue curve $[S(\Delta y; 0.007\lambda, n) - S(\Delta y; 0.005\lambda, n)]$.

Noisy measurements of two slab configurations with minuscule differences in the film's refractive index n and thickness L can be separated with higher confidence if their error bars do not overlap. This is shown in the magnified data in Fig. 4.2(a) and (b). In other words, separability is achieved when the difference of the noiseless data is larger than the sum of half of the respective error bar lengths for each measurement. This is further demonstrated in Fig. 4.2(c) and (d), where we calculate the difference

of the two curves in Fig. 4.2(a) and (b), with the same error bars superimposed at each data point. In Fig. 4.2(c), the red curve sets $S(\Delta y; L, 1.95)$ to zero as a reference, and the blue curve represents $[S(\Delta y; L, 2.00) - S(\Delta y; L, 1.95)]$. The same is repeated in Fig. 4.2(d), where the red curve sets $S(\Delta y; 0.005\lambda, n)$ to zero, and the blue curve represents $[S(\Delta y; 0.007\lambda, n) - S(\Delta y; 0.005\lambda, n)]$. From Fig. 4.2(c) and (d), we see that there exist multiple data points where there are non-overlapping error bars, which can then be used as leverage to distinguish between two different noisy measurements, thus demonstrating sensitivity to small differences in film refractive indices and film thicknesses. Note that the data shown in Fig. 4.2 represents motion span of one period, and repeats as the object continues its motion in the structured field.

4.2 Thin Film Characterization

We demonstrate a straightforward application for the sensitivity provided with motion in structured illumination by reconstructing the film's thickness (L) and refractive index (n) on top of a slab with known optical properties using the system in Fig. 4.1. Utilizing the measurements obtained this way, we can use a cost function to find parameters of interest by comparing the measurement with forward calculations over a range of different combinations of L and n . We denote $\mathbf{f}(L, n)$ as the array of calculated data, where each entry represents the data at each Δy location obtained from the forward model $S(\Delta y; L, n)$, and \mathbf{y} as the array of simulated noisy measurements with presumably unknown true thickness, L_t , and refractive index, n_t . Both $\mathbf{f}(L, n)$ and \mathbf{y} have dimensions equal to the total number of positions, K , that the object has moved in the structured field. We denote \mathbf{y}_k as the k th element in array \mathbf{y} , and $\mathbf{f}_k(L, n)$ as the k th element in $\mathbf{f}(L, n)$. Note that each entry of \mathbf{y} can be generated using the noise model described previously, with $\mathbf{y}_k = \mathbf{f}_k(L_t, n_t) + \sigma \times N(0, 1)$, where

$N(0, 1)$ represents a normal distribution with zero mean and unit standard deviation. We can then determine the estimated value of \hat{L} and \hat{n} from

$$(\hat{L}, \hat{n}) = \arg \min_{L, n} \sum_{k=1}^K |\mathbf{y}_k - \mathbf{f}_k(L, n)|. \quad (4.1)$$

Here we chose an L1-norm as our cost function to illustrate the potential of this application due to its robustness and resistance to outliers in data. However, an L2-norm cost function combined with other optimization algorithms can be considered using the data obtained from this method. The forward calculations were made for a range of possible thicknesses (L) and refractive indices (n) that encompasses L_t and n_t . Consider a hypothetical experiment from a film structure with $L_t = 0.006\lambda$ and $n_t = 1.72$, with a SNR = 30 dB. The calculated costs from (4.1) for each combination of $L \in [0.002\lambda, 0.022\lambda]$ with step increments of 0.002λ , and $n \in [1.62, 1.98]$ with step increments of 0.04 (resulting in an 11x11 grid), is shown in the top left plot of Fig. 4.3. The cost is at the minimum when $\hat{L} = 0.006\lambda$ and $\hat{n} = 1.72$, as indicated by the red circle on the grid, demonstrating a correct estimation of the thickness and refractive index from noisy data. This accurate reconstruction is possible if the true thickness and refractive index is assumed to fall within the range of calculated configurations in the grid.

A multi-resolution approach can be applied, significantly decreasing the calculation time while maintaining the same resolution when scanning over a larger search range of L_t and n_t . This is demonstrated in Fig. 4.3, where we start from the top right plot. The cost is calculated and minimized on a coarse 5x5 grid with an increased range of parameters, where $L \in [0.002\lambda, 0.13\lambda]$, roughly half of the entire sample, and $n \in [1, 3.56]$. The cost is then calculated iteratively on a smaller region of interest and on a finer grid that zooms in at the point of minimum cost and extends a distance equal to the grid spacing from the previous iteration, as shown by following the arrows in Fig. 4.3. This procedure is repeated five times until the step increments of the film thickness on the grid reaches 0.002λ , which is where the measurements remain separable given a 30 dB SNR.

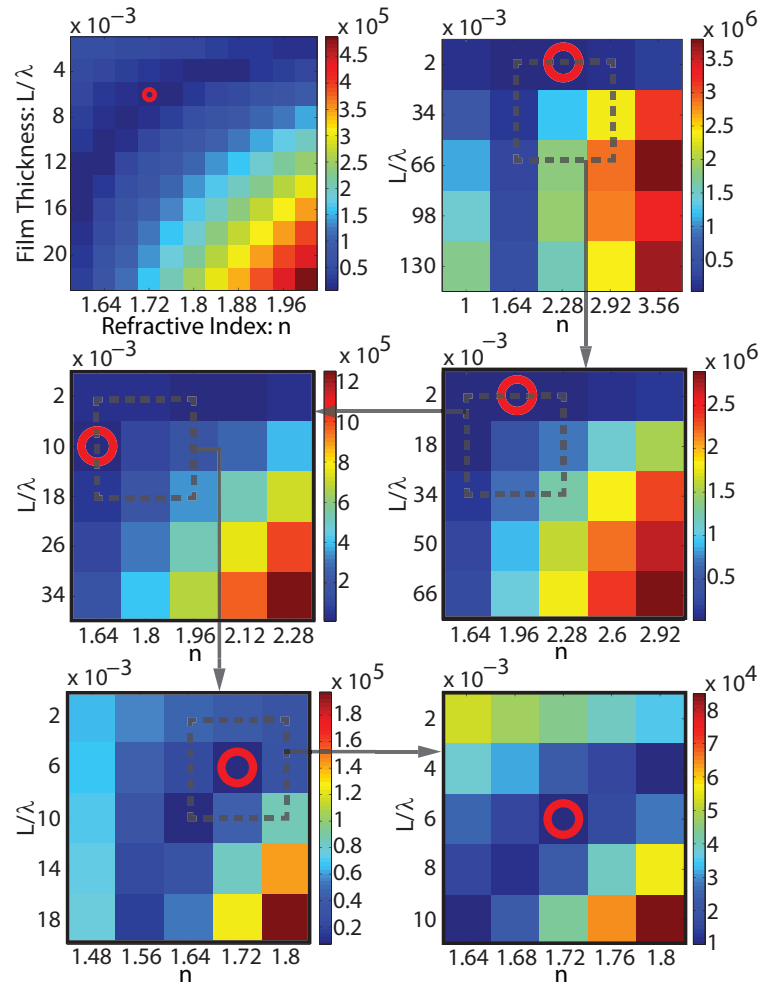


Fig. 4.3. Calculated costs for a thin film substrate by comparing the simulated noisy experimental measurements with forward calculations of different film configurations without multiresolution (top left), and with multiresolution (starting from top right and following the arrows). The film substrate used in the simulated experiment has a film thickness $L_t = 0.006\lambda$ and refractive index $n_t = 1.72$. Without multiresolution, forward calculations were made for different combinations of film thicknesses $L \in [0.002\lambda, 0.022\lambda]$ with step increments of 0.002λ , and refractive indices $n \in [1.62, 1.98]$ with step increments of 0.04 , resulting in an 11×11 grid. The cost is minimized at the correct parameters where $\hat{L} = 0.006\lambda$ and $\hat{n} = 1.72$. When using a multiresolution approach, forward calculations were made on a coarse 5×5 grid with a significantly increased range of values of $L \in [0.002\lambda, 0.13\lambda]$ and $n \in [1, 3.56]$. The cost is calculated iteratively on zoomed in regions of interest (following the arrows) that encompasses the the point of minimum cost.

4.3 Resolution

Since the simulated experimental measurements are noisy, the reconstructed film thickness and refractive index will fall within a distribution. To evaluate the efficacy of this characterization method we use the same film substrate structure, and generate 500 noisy independent simulated experimental measurements for a given SNR. The 500 sets of reconstructed thicknesses and refractive indices were then obtained from these independent measurements, which allows us to obtain a statistical distribution of the reconstructed values for the given SNR. This is repeated for different values of SNR to demonstrate the performance at different SNR values and is shown in Fig. 4.4. Figure 4.4 shows box plots of the distribution of reconstructed thickness and refractive index at different values of SNR. For each SNR, the top and bottom edges of the box represent the upper and lower quartile of reconstructed values, the whiskers extend to the minimum and the maximum values and the red dots represent outliers (defined as less than the first quartile or greater than the third quartile by more than 1.5 times the interquartile range). The red dashed line in both plots represents the median of the reconstructed values at each SNR and is identical to the true film thickness, L_t , and refractive index, n_t . In Fig. 4.4(a), the length of the box is skewed upwards and asymmetric about the median. This is due to the boundary limits of the possible reconstructed values of the thickness, i.e., the reconstructed thickness cannot go below 0.002λ . In Fig. 4.4, it is shown here that for both reconstructions of film thickness and refractive index, as the SNR increases, with the exception of several outliers, the size of the boxes and whiskers gradually decrease and converge to the median at around 32dB, depicting a convergence to L_t and n_t .

4.4 Detectability

The limitations of this method is further investigated in terms of sensitivity for the cases of very thin films and films with low index contrast relative to the slab. We consider the same film-substrate structure shown in Fig. 4.1, but for various sets

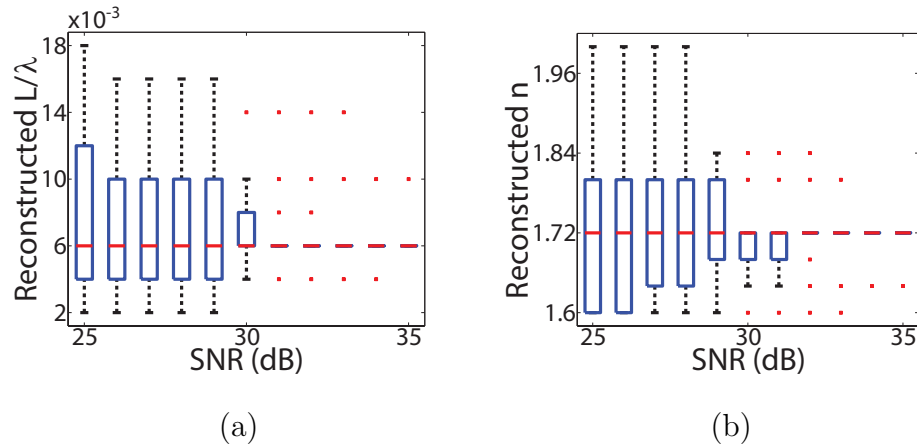


Fig. 4.4. 500 independent measurements were made at different SNR values to calculate a distribution of reconstructed values of $L/1000\lambda$ and n , representing uncertainty in the reconstruction of thin film parameters. (a) Box plots of the distribution of reconstructed film thicknesses for different SNR values. Note that the y -axis is on the scale of 10^{-3} . (b) Box plots of the distribution of reconstructed refractive indices. The top edge of the box represent the upper quartile of the reconstructed values, and the bottom edge represent the lower quartile. The whiskers extend to the upper and lower extremes, and the red dots represent outliers. In both plots, the median (red dashed line) obtained from the set of reconstructed values is equal to the the true film thickness and refractive index, L_t and n_t .

of combinations of thin film thicknesses, and differences in refractive index (Δn), when compared to the case of a slab with the film having the same material as the slab. For a given SNR, we generated 10^5 sets of measurement data for each unique film parameter combination with $L \in [0.001\lambda, 0.01\lambda]$ (increments of 0.001λ) and $\Delta n \in [0.02, 0.2]$ (increments of 0.02). We use Eq. 4.1 to determine whether the estimated parameters detects the presence of a thin film or returns a slab with no film present due to measurement noise. This would give us the detectability for each film parameter combination (percentage of correct reconstructions showing the thin film present). Contours can then be obtained for when the detectability is at least 99.99%. The contours were then fitted to a two-term power series model ($y = ax^b + c$, in this case, y and x are L/λ and Δn , respectively, a and b are the fitted coefficients), and is plotted in Fig. 4.5. In Fig. 4.5(a), fitted contours were drawn for SNR values of 35 dB, 30 dB, and 25 dB, which are represented as the dashed black line, solid red line, and dashed-dotted blue line, respectively. In other words, the area to the right and above the curve represents the parameter space of the thin film that can be reconstructed and distinguished from measurements of a film-less slab. It can be seen from Fig. 4.5(a) that with a higher SNR, it is possible to detect a thinner film with lower optical contrast compared to the slab. For example, in the case of a 30 dB SNR, 0.002λ is the lower limit for reconstruction and resolution in terms of film thickness for particular values of n , while 0.04 is the lower limit for contrast in refractive index for particular values of L . In Fig. 4.5(b), contours for different number of positions, K , are plotted to investigate how K affects the efficacy of the method while fixing the SNR to 30 dB. In both plots, the solid red curve represents identical parameters ($K = 21$, SNR = 30). The solid red curve, the dashed black curve, and the dashed-dotted blue line is for K equals 21, 11, and 5, respectively. Increasing the number of steps that the slab moves within the cavity gives more information and in turn higher detectability.

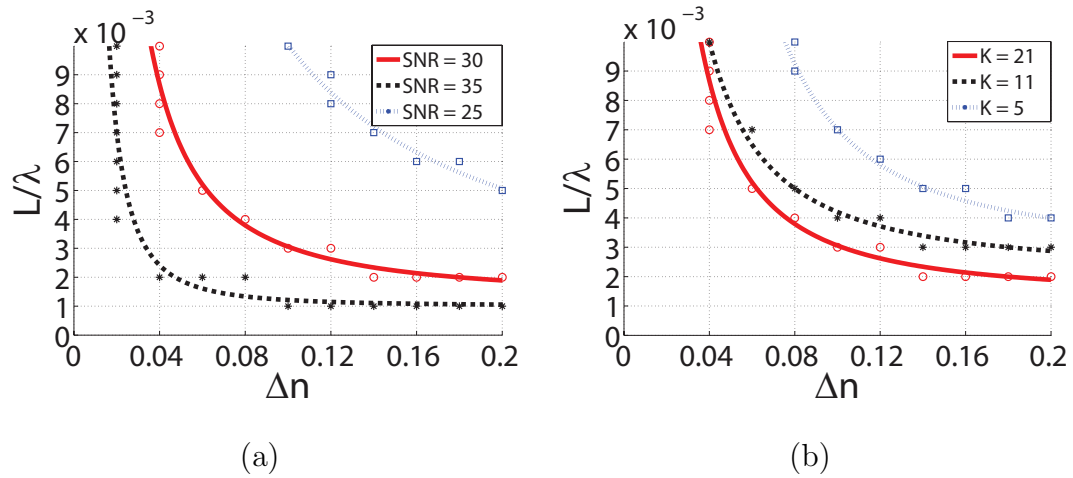


Fig. 4.5. Minimum detectability of very thin films with low index contrast relative to the optical properties of the slab. The region to the right and above of each curves represent detectability above 99.99% for when a thin film is present from noisy measurement data. (a) The dashed black, solid red, and dashed-dotted blue curves correspond to 35 dB, 30 dB, and 25 dB, respectively. (b) At a SNR = 30 dB, the solid red, dashed black, and dashed-dotted blue curves correspond to when the number of positions, K , equals 21, 11, 5, respectively.

4.5 Conclusion

In conclusion, we have presented a method to obtain the optical parameters and thickness of a thin film on a substrate using motion in structured illumination. Several changes to experiments using this method can be also be considered. For example, reflective measurements can be used when the substrate is non transparent or above band gap light is used, and in that case the substrate itself can serve as a mirror to form structured illumination. Other ways of generating structured illumination can also be applied, such as spatial light modulators, therefore removing the need for a Fabry-Perot cavity. Alternatively, the standing wave could be scanned by controlling the incident field and making measurements with a fixed detector. In terms of forward calculations, analytical solutions can also be used instead of numerical solutions. As for performing optimization of cost functions, the iterative coordinate descent algorithm with multigrid could be applied, due to its demonstrated capabilities of avoiding local minima while reducing the computational burden when solving non-linear optimization problems [90].

5. FUTURE DIRECTIONS

5.1 Whole-Brain Fluorescent Imaging

In Chapters 2 and 3, we have shown that localization through SRDOI is a powerful tool for retrieving high spatial and temporal resolution information of fluorescent emitters in scattering media. One potential future application of SRDOI is brain imaging [83, 85, 86]. Current whole-brain imaging methods, such as PET and MRI, image the brain by detecting associated changes in blood flow, specifically through blood oxygen level contrast [91–94]. However, they do not provide direct access to neurons, i.e., they measure secondary parameters. Optical methods such as two-photon microscopy offer more direct access to a wider range of neurobiological information through optical contrast agents, but they are limited to applications near the surface [95–98]. Understanding the functionality of the brain requires imaging of the whole brain *in vivo*, which is not possible with available optical imaging methods.

Signaling among neurons is accompanied by an increase in the local concentration of calcium, which can modulate the emission of fluorescent calcium reporters within the brain [84, 87]. Each neuron can be treated as a fluorescent source that, for example, emits photons in response to calcium channels opening. This provides a direct indication of neuron activity. In this case, data captured with an intensified CCD camera or a fiber array over an appropriate integration time can yield information that could allow neurons or clusters of neurons to be localized with SRDOI. In principle, this could provide an image of a whole animal brain or a brain region *in vivo* at a resolution of tens of micrometers. These images would provide new information on how the brain encodes perceived information into neural activity, and how neural circuits interact with different brain areas. Correlation maps with such data should prove useful for studying neurological diseases and developing treatments [88].

5.2 Film Characterization and Defect Detection

In Chapter 4, we showed that intensity measurements obtained as a function of object position inside a structured field provide information on the material and subwavelength-scale information of a thin film on a substrate. We also demonstrated the application of thin film characterization through simultaneous reconstruction of the refractive index and the thickness of a thin film on a slab to nanometer precision. With sensitivity to differential changes in parameters, the application space can be further expanded to characterize a layer of material within a well-characterized stack of multiple layers of different materials, or to detect the presence of an inhomogeneity (defect) located within a stack of multiple layers by comparing the measurement with that of an inhomogeneity-free stack. It may thus be possible to determine the presence of a defect in a semiconductor. However, the ability to characterize inhomogeneities still depends on the SNR, size, and contrast between the inhomogeneity and the background layer. We have shown that, given an SNR of 30 dB with the arrangement considered, a resolution of $L = 0.002\lambda$ and a refractive index change of $\Delta n = 0.04$ can be achieved for detection of a thin film. This work presents a starting point for investigating the resolution limit for small inhomogeneities in slabs for future work. Other optimization methods can be explored and used in conjunction with this approach. The method also has the potential to be extended to retrieve the imaginary component of the refraction index by introducing a third unknown variable into the cost function. Note that, at this stage, the results presented do not take surface roughness into account, which would be another step.

REFERENCES

REFERENCES

- [1] M. S. Patterson, B. Chance, and B. C. Wilson, "Time resolved reflectance and transmittance for the non-invasive measurement of tissue optical properties," *Applied Optics*, vol. 28, no. 12, pp. 2331–2336, 1989.
- [2] M. O’leary, D. Boas, B. Chance, and A. Yodh, "Refraction of diffuse photon density waves," *Phys. Rev. Lett.*, vol. 69, no. 18, p. 2658, 1992.
- [3] B. C. Wilson, E. M. Sevick, M. S. Patterson, and B. Chance, "Time-dependent optical spectroscopy and imaging for biomedical applications," *Proceedings of the IEEE*, vol. 80, no. 6, pp. 918–930, 1992.
- [4] S. R. Arridge and J. C. Hebden, "Optical imaging in medicine: Ii. modelling and reconstruction," *Phys. Med. Biol.*, vol. 42, no. 5, p. 841, 1997.
- [5] E. Abbe, "Beiträge zur theorie des mikroskops und der mikroskopischen wahrnehmung," *Arch. Mikr. Anat.*, vol. 9, no. 1, pp. 413–418, 1873.
- [6] D. Huang, E. A. Swanson, C. P. Lin, J. S. Schuman, W. G. Stinson, W. Chang, M. R. Hee, T. Flotte, K. Gregory, C. A. Puliafito, and J. G. Fujimoto, "Optical coherence tomography," *Science*, vol. 254, no. 5035, p. 1178, 1991.
- [7] F. Helmchen and W. Denk, "Deep tissue two-photon microscopy," *Nat. Methods*, vol. 2, no. 12, pp. 932–940, 2005.
- [8] C. Gonatas, M. Ishii, J. S. Leigh, and J. C. Schotland, "Optical diffusion imaging using a direct inversion method," *Phys. Rev. E*, vol. 52, no. 4, p. 4361, 1995.
- [9] J. Ripoll, R. B. Schulz, and V. Ntziachristos, "Free-space propagation of diffuse light: theory and experiments," *Phys. Rev. Lett.*, vol. 91, no. 10, p. 103901, 2003.
- [10] A. Gibson, J. Hebden, and S. R. Arridge, "Recent advances in diffuse optical imaging," *Phys. Med. Biol.*, vol. 50, no. 4, p. R1, 2005.
- [11] J. C. Ye, K. J. Webb, C. A. Bouman, and R. P. Millane, "Optical diffusion tomography by iterative coordinate descent optimization in a Bayesian framework," *J. Opt. Soc. Am. A*, vol. 16, no. 10, pp. 2400–2412, October 1999.
- [12] D. L. Everitt, S.-p. Wei, and X. Zhu, "Analysis and optimization of a diffuse photon optical tomography of turbid media," *Phys. Rev. E*, vol. 62, no. 2, p. 2924, 2000.
- [13] V. A. Markel and J. C. Schotland, "Symmetries, inversion formulas, and image reconstruction for optical tomography," *Phys. Rev. E*, vol. 70, no. 5, p. 056616, 2004.

- [14] V. Ntziachristos and R. Weissleder, "Charge-coupled-device based scanner for tomography of fluorescent near-infrared probes in turbid media," *Med. Phys.*, vol. 29, no. 5, pp. 803–809, 2002.
- [15] A. B. Milstein, S. Oh, K. J. Webb, C. A. Bouman, Q. Zhang, D. A. Boas, and R. P. Millane, "Fluorescence optical diffusion tomography," *Appl. Opt.*, vol. 42, no. 16, pp. 3081–3094, Jun. 2003.
- [16] E. H. R. Tsai, B. Z. Bentz, V. Chelvam, V. Gaind, K. J. Webb, and P. S. Low, "In vivo mouse fluorescence imaging for folate-targeted delivery and release kinetics," *Biomed. Opt. Express*, vol. 5, no. 8, pp. 2662–2678, 2014.
- [17] J. Skoch, A. K. Dunn, B. T. Hyman, and B. J. Bacskai, "Development of an optical approach for noninvasive imaging of alzheimer's disease pathology," *J. Biomed. Opt.*, vol. 10, no. 1, p. 011007, 2005.
- [18] V. Ntziachristos, J. Ripoll, L. V. Wang, and R. Weissleder, "Looking and listening to light: the evolution of whole-body photonic imaging," *Nat. Biotechnol.*, vol. 23, no. 3, pp. 313–320, 2005.
- [19] E. L. Hull, M. G. Nichols, and T. H. Foster, "Localization of luminescent inhomogeneities in turbid media with spatially resolved measurements of cw diffuse luminescence emittance," *Appl. Opt.*, vol. 37, no. 13, pp. 2755–2765, 1998.
- [20] M. Pfister and B. Scholz, "Localization of fluorescence spots with space-space music for mammographylike measurement systems," *J. Biomed. Opt.*, vol. 9, no. 3, pp. 481–487, 2004.
- [21] A. B. Milstein, M. D. Kennedy, P. S. Low, C. A. Bouman, and K. J. Webb, "Statistical approach for detection and localization of a fluorescing mouse tumor in intralipid," *Appl. Opt.*, vol. 44, no. 12, pp. 2300–2310, 2005.
- [22] J.-P. L'Huillier and F. Vaudelle, "Improved localization of hidden fluorescent objects in highly scattering slab media based on a two-way transmittance determination," *Opt. Exp.*, vol. 14, no. 26, pp. 12 915–12 929, 2006.
- [23] Y. Chen, G. Zheng, Z. Zhang, D. Blessington, M. Zhang, H. Li, Q. Liu, L. Zhou, X. Intes, S. Achilefu, and B. Chance, "Metabolism-enhanced tumor localization by fluorescence imaging: in vivo animal studies," *Opt. Lett.*, vol. 28, no. 21, pp. 2070–2072, 2003.
- [24] M. G. L. Gustafsson, "Surpassing the lateral resolution limit by a factor of two using structured illumination microscopy," *J. Microsc.*, vol. 198, no. 2, pp. 82–87, 2000.
- [25] S. W. Hell and J. Wichmann, "Breaking the diffraction resolution limit by stimulated emission: stimulated-emission-depletion fluorescence microscopy," *Opt. Lett.*, vol. 19, no. 11, pp. 780–782, 1994.
- [26] E. Betzig, G. H. Patterson, R. Sougrat, O. W. Lindwasser, S. Olenych, J. S. Bonifacino, M. W. Davidson, J. Lippincott-Schwartz, and H. F. Hess, "Imaging intracellular fluorescent proteins at nanometer resolution," *Science*, vol. 313, no. 5793, pp. 1642–1645, 2006.

- [27] M. J. Rust, M. Bates, and X. Zhuang, “Sub-diffraction-limit imaging by stochastic optical reconstruction microscopy (STORM),” *Nat. Meth.*, vol. 3, no. 10, pp. 793–796, 2006.
- [28] V. Ntziachristos, C. Bremer, and R. Weissleder, “Fluorescence imaging with near-infrared light: new technological advances that enable in vivo molecular imaging,” *Eur. Radiol.*, vol. 13, no. 1, pp. 195–208, 2003.
- [29] J. R. Lakowicz, *Principles of Fluorescence Spectroscopy*. Springer, 2009.
- [30] S. A. Hilderbrand and R. Weissleder, “Near-infrared fluorescence: application to in vivo molecular imaging,” *Curr. Opin. Chem. Biol.*, vol. 14, no. 1, pp. 71–79, 2010.
- [31] J. White, W. Amos, and M. Fordham, “An evaluation of confocal versus conventional imaging of biological structures by fluorescence light microscopy.” *J. Cell. Biol.*, vol. 105, no. 1, pp. 41–48, 1987.
- [32] A. Gandjbakhche, R. Nossal, and R. Bonner, “Resolution limits for optical transillumination of abnormalities deeply embedded in tissues,” *Med. Phys.*, vol. 21, no. 2, pp. 185–191, 1994.
- [33] J. Ripoll, M. Nieto-Vesperinas, and R. Carminati, “Spatial resolution of diffuse photon density waves,” *J. Opt. Soc. Am. A*, vol. 16, no. 6, pp. 1466–1476, 1999.
- [34] B. W. Pogue, T. O. McBride, U. L. Osterberg, and K. D. Paulsen, “Comparison of imaging geometries for diffuse optical tomography of tissue,” *Opt. Exp.*, vol. 4, no. 8, pp. 270–286, 1999.
- [35] E. E. Graves, J. Ripoll, R. Weissleder, and V. Ntziachristos, “A submillimeter resolution fluorescence molecular imaging system for small animal imaging,” *Med. Phys.*, vol. 30, no. 5, pp. 901–911, 2003.
- [36] D. Boas, K. Chen, D. Grebert, and M. Franceschini, “Improving the diffuse optical imaging spatial resolution of the cerebral hemodynamic response to brain activation in humans,” *Opt. Lett.*, vol. 29, no. 13, pp. 1506–1508, 2004.
- [37] L. Zhao, V. K. Lee, S.-S. Yoo, G. Dai, and X. Intes, “The integration of 3-D cell printing and mesoscopic fluorescence molecular tomography of vascular constructs within thick hydrogel scaffolds,” *Biomaterials*, vol. 33, no. 21, pp. 5325–5332, 2012.
- [38] M. S. Ozturk, V. K. Lee, L. Zhao, G. Dai, and X. Intes, “Mesoscopic fluorescence molecular tomography of reporter genes in bioprinted thick tissue,” *J. Biomed. Opt.*, vol. 18, no. 10, pp. 100 501–100 501, 2013.
- [39] H. Fujiwara, *Spectroscopic Ellipsometry: Principles and Applications*. John Wiley & Sons, 2007.
- [40] S.-W. Kim and G.-H. Kim, “Thickness-profile measurement of transparent thin-film layers by white-light scanning interferometry,” *Applied Optics*, vol. 38, no. 28, pp. 5968–5973, 1999.
- [41] K. J. Webb, Y. Chen, and T. A. Smith, “Object motion with structured optical illumination as a basis for far-subwavelength resolution,” *Physical Review Applied*, vol. 6, no. 2, p. 024020, 2016.

- [42] J. A. Newman, Q. Luo, and K. J. Webb, “Imaging hidden objects with spatial speckle intensity correlations over object position,” *Phys. Rev. Lett.*, vol. 116, no. 7, p. 073902, 2016.
- [43] B. Z. Bentz, D. Lin, and K. J. Webb, “Superresolution diffuse optical imaging by localization of fluorescence,” *Physical Review Applied*, vol. 10, no. 3, p. 034021, 2018.
- [44] X. Li, M. O’Leary, D. Boas, B. Chance, and A. Yodh, “Fluorescent diffuse photon density waves in homogeneous and heterogeneous turbid media: analytic solutions and applications,” *Appl. Opt.*, vol. 35, no. 19, pp. 3746–3758, 1996.
- [45] S. Bélanger, M. Abran, X. Intes, C. Casanova, and F. Lesage, “Real-time diffuse optical tomography based on structured illumination,” *J. Biomed. Opt.*, vol. 15, no. 1, pp. 016 006–016 006, 2010.
- [46] C. L. Matson, “Deconvolution-based spatial resolution in optical diffusion tomography,” *Appl. Opt.*, vol. 40, no. 31, pp. 5791–5801, 2001.
- [47] X. Li, T. Durduran, A. Yodh, B. Chance, and D. Pattanayak, “Diffraction tomography for biochemical imaging with diffuse-photon density waves,” *Opt. Lett.*, vol. 22, no. 8, pp. 573–575, 1997.
- [48] X. Zhou, Y. Fan, Q. Hou, H. Zhao, and F. Gao, “Spatial-frequency-compression scheme for diffuse optical tomography with dense sampling dataset,” *Appl. Opt.*, vol. 52, no. 9, pp. 1779–1792, 2013.
- [49] J. Moon, R. Mahon, M. Duncan, and J. Reintjes, “Resolution limits for imaging through turbid media with diffuse light,” *Opt. Lett.*, vol. 18, no. 19, pp. 1591–1593, 1993.
- [50] B. W. Pogue and K. D. Paulsen, “High-resolution near-infrared tomographic imaging simulations of the rat cranium by use of a priori magnetic resonance imaging structural information,” *Opt. Lett.*, vol. 23, no. 21, pp. 1716–1718, 1998.
- [51] V. Ntziachristos, A. Yodh, M. D. Schnall, and B. Chance, “MRI-guided diffuse optical spectroscopy of malignant and benign breast lesions,” *Neoplasia*, vol. 4, no. 4, pp. 347–354, 2002.
- [52] J. Ripoll, V. Ntziachristos, R. Carminati, and M. Nieto-Vesperinas, “Kirchhoff approximation for diffusive waves,” *Phys. Rev. E*, vol. 64, no. 5, p. 051917, 2001.
- [53] M. Schweiger and S. Arridge, “The Toast++ software suite for forward and inverse modeling in optical tomography,” *J. Biomed. Opt.*, vol. 19, no. 4, pp. 040 801–040 801, 2014.
- [54] R. C. Haskell, L. O. Svaasand, T.-T. Tsay, T.-C. Feng, B. J. Tromberg, and M. S. McAdams, “Boundary conditions for the diffusion equation in radiative transfer,” *J. Opt. Soc. Am. A*, vol. 11, no. 10, pp. 2727–2741, 1994.
- [55] G. Cao, V. Gaind, C. A. Bouman, and K. J. Webb, “Localization of an absorbing inhomogeneity in a scattering medium in a statistical framework,” *Opt. Lett.*, vol. 32, no. 20, pp. 3026–3028, 2007.

- [56] A. Brandt, *Multigrid Techniques: 1984 Guide, with Applications to Fluid Dynamics*. Sankt Augustin, Germany: GMD-Studien, 1984.
- [57] J. C. Ye, C. A. Bouman, K. J. Webb, and R. P. Millane, “Nonlinear multigrid algorithms for Bayesian optical diffusion tomography,” *IEEE Trans. Image Process.*, vol. 10, no. 6, pp. 909–922, 2001.
- [58] R. E. Thompson, D. R. Larson, and W. W. Webb, “Precise nanometer localization analysis for individual fluorescent probes,” *Biophys. J.*, vol. 82, no. 5, pp. 2775–2783, 2002.
- [59] X. Michalet, “Mean square displacement analysis of single-particle trajectories with localization error: Brownian motion in an isotropic medium,” *Phys. Rev. E*, vol. 82, no. 4, p. 041914, 2010.
- [60] T. D. Lacoste, X. Michalet, F. Pinaud, D. S. Chemla, A. P. Alivisatos, and S. Weiss, “Ultrahigh-resolution multicolor colocalization of single fluorescent probes,” *Proc. Natl. Acad. Sci.*, vol. 97, no. 17, pp. 9461–9466, 2000.
- [61] S. T. Hess, T. P. Girirajan, and M. D. Mason, “Ultra-high resolution imaging by fluorescence photoactivation localization microscopy,” *Biophys. J.*, vol. 91, no. 11, pp. 4258–4272, 2006.
- [62] F. Balzarotti, Y. Eilers, K. C. Gwosch, A. H. Gynnå, V. Westphal, F. D. Stefani, J. Elf, and S. W. Hell, “Nanometer resolution imaging and tracking of fluorescent molecules with minimal photon fluxes,” *Science*, vol. 355, no. 6325, pp. 606–612, 2017.
- [63] A. Papoulis and S. U. Pillai, *Probability, Random Variables, and Stochastic Processes*. Tata McGraw-Hill Education, 2002.
- [64] C. A. Thompson, K. J. Webb, and A. M. Weiner, “Diffusive media characterization with laser speckle,” *Appl. Opt.*, vol. 36, no. 16, pp. 3726–3734, 1997.
- [65] M. Schweiger, S. R. Arridge, and D. T. Delpy, “Application of the finite-element method for the forward and inverse models in optical tomography,” *J. Math. Imaging Vision*, vol. 3, no. 3, pp. 263–283, 1993.
- [66] J. Heino, S. Arridge, J. Sikora, and E. Somersalo, “Anisotropic effects in highly scattering media,” *Phys. Rev. E*, vol. 68, no. 3, p. 031908, 2003.
- [67] V. Pera, E. Zettergren, D. H. Brooks, and M. Niedre, “Maximum likelihood tomographic reconstruction of extremely sparse solutions in diffuse fluorescence flow cytometry,” *Opt. Lett.*, vol. 38, no. 13, pp. 2357–2359, 2013.
- [68] K. T. Shimizu, R. G. Neuhauser, C. A. Leatherdale, S. A. Empedocles, W. Woo, and M. G. Bawendi, “Blinking statistics in single semiconductor nanocrystal quantum dots,” *Phys. Rev. B*, vol. 63, no. 20, p. 205316, 2001.
- [69] H. Blom and J. Widengren, “Stimulated emission depletion microscopy,” *Chem. Rev.*, 2017.
- [70] M. Xu and L. V. Wang, “Universal back-projection algorithm for photoacoustic computed tomography,” *Phys. Rev. E*, vol. 71, no. 1, p. 016706, 2005.

- [71] M. Cheney, D. Isaacson, and J. C. Newell, “Electrical impedance tomography,” *SIAM review*, vol. 41, no. 1, pp. 85–101, 1999.
- [72] R. G. Pratt, “Seismic waveform inversion in the frequency domain, Part 1: Theory and verification in a physical scale model,” *Geophysics*, vol. 64, no. 3, pp. 888–901, 1999.
- [73] T. Rubæk, P. M. Meaney, P. Meincke, and K. D. Paulsen, “Nonlinear microwave imaging for breast-cancer screening using gauss–newton’s method and the cgls inversion algorithm,” *IEEE T. Antenn. Propag.*, vol. 55, no. 8, pp. 2320–2331, 2007.
- [74] B. Z. Bentz, D. Lin, J. A. Patel, and K. J. Webb, “Multiresolution localization with temporal scanning for super-resolution diffuse optical imaging of fluorescence,” *IEEE Trans on Image Process.*, vol. 29, pp. 830–842, 2019.
- [75] H. Jiang, K. D. Paulsen, U. L. Osterberg, B. W. Pogue, and M. S. Patterson, “Optical image reconstruction using frequency domain data: simulations and experiments,” *J. Opt. Soc. Am. A*, vol. 13, no. 2, pp. 253–266, Feb 1996.
- [76] S. R. Arridge, “Optical tomography in medical imaging,” *Inverse Probl.*, vol. 15, no. 2, p. R41, 1999.
- [77] H. Schau and A. Robinson, “Passive source localization employing intersecting spherical surfaces from time-of-arrival differences,” *IEEE Trans. Acoust. Speech*, vol. 35, no. 8, pp. 1223–1225, 1987.
- [78] I. Ziskind and M. Wax, “Maximum likelihood localization of multiple sources by alternating projection,” *IEEE Trans. Acoust. Speech*, vol. 36, no. 10, pp. 1553–1560, 1988.
- [79] I. Gannot, A. Garashi, G. Gannot, V. Chernomordik, and A. Gandjbakhche, “In vivo quantitative three-dimensional localization of tumor labeled with exogenous specific fluorescence markers,” *Appl. Opt.*, vol. 42, no. 16, pp. 3073–3080, 2003.
- [80] M. Xu and L. V. Wang, “Universal back-projection algorithm for photoacoustic computed tomography,” *Phys. Rev. E*, vol. 71, p. 016706, 2005.
- [81] R. G. Pratt, “Seismic waveform inversion in the frequency domain, part 1: Theory and verification in a physical scale model,” *GÉOPHYSICS*, vol. 64, no. 3, pp. 888–901, 1999.
- [82] T. Rubæk, P. M. Meaney, P. Meincke, and K. D. Paulsen, “Nonlinear microwave imaging for breast-cancer screening using gauss–newton’s method and the cgls inversion algorithm,” *IEEE Trans. Antennas Propagat.*, vol. 55, no. 8, pp. 2320–2331, 2007.
- [83] M. Scherg, “Functional imaging and localization of electromagnetic brain activity,” *Brain Topogr.*, vol. 5, no. 2, pp. 103–111, 1992.
- [84] R. Yasuda, E. A. Nimchinsky, V. Scheuss, T. A. Pologruto, T. G. Oertner, B. L. Sabatini, and K. Svoboda, “Imaging calcium concentration dynamics in small neuronal compartments,” *Sci. STKE*, vol. 2004, no. 219, p. pl5, 2004.

- [85] R. Prevedel, Y.-G. Yoon, M. Hoffmann, N. Pak, G. Wetzstein, S. Kato, T. Schrödel, R. Raskar, M. Zimmer, E. S. Boyden, and A. Vaziri, “Simultaneous whole-animal 3D imaging of neuronal activity using light-field microscopy,” *Nat. Meth.*, vol. 11, no. 7, pp. 727–730, 2014.
- [86] A. T. Eggebrecht, S. L. Ferradal, A. Robichaux-Viehoever, M. S. Hassanpour, H. Dehghani, A. Z. Snyder, T. Hershey, and J. P. Culver, “Mapping distributed brain function and networks with diffuse optical tomography,” *Nat. Photon.*, vol. 8, no. 6, pp. 448–454, 2014.
- [87] M. L. Castanares, V. Gautam, J. Drury, H. Bachor, and V. R. Daria, “Efficient multi-site two-photon functional imaging of neuronal circuits,” *Biomed. Opt. Express*, vol. 7, no. 12, pp. 5325–5334, 2016.
- [88] E. Bullmore and O. Sporns, “Complex brain networks: graph theoretical analysis of structural and functional systems,” *Nat. Rev. Neurosci.*, vol. 10, no. 3, pp. 186–198, 2009.
- [89] *COMSOL Multiphysics v. 5.4*. Stockholm, Sweden: COMSOL AB.
- [90] J. C. Ye, K. J. Webb, C. A. Bouman, and R. P. Millane, “Optical diffusion tomography by iterative-coordinate-descent optimization in a bayesian framework,” *J. Opt. Soc. Am. A*, vol. 16, no. 10, pp. 2400–2412, 1999.
- [91] K. K. Kwong, J. W. Belliveau, D. A. Chesler, I. E. Goldberg, R. M. Weisskoff, B. P. Poncelet, D. N. Kennedy, B. E. Hoppel, M. S. Cohen, and R. Turner, “Dynamic magnetic resonance imaging of human brain activity during primary sensory stimulation.” *Proc. Natl. Acad. Sci.*, vol. 89, no. 12, pp. 5675–5679, 1992.
- [92] D. Malonek, U. Dirnagl, U. Lindauer, K. Yamada, I. Kanno, and A. Grinvald, “Vascular imprints of neuronal activity: relationships between the dynamics of cortical blood flow, oxygenation, and volume changes following sensory stimulation,” *Proc. Natl. Acad. Sci.*, vol. 94, no. 26, pp. 14 826–14 831, 1997.
- [93] D. J. Heeger and D. Ress, “What does fMRI tell us about neuronal activity?” *Nat. Rev. Neurosci.*, vol. 3, no. 2, pp. 142–151, 2002.
- [94] M. E. Raichle and M. A. Mintun, “Brain work and brain imaging,” *Annu. Rev. Neurosci.*, vol. 29, pp. 449–476, 2006.
- [95] F. Helmchen and W. Denk, “Deep tissue two-photon microscopy,” *Nat. Meth.*, vol. 2, no. 12, pp. 932–940, 2005.
- [96] J. W. Wang, A. M. Wong, J. Flores, L. B. Vosshall, and R. Axel, “Two-photon calcium imaging reveals an odor-evoked map of activity in the fly brain,” *Cell*, vol. 112, no. 2, pp. 271–282, 2003.
- [97] F. Helmchen, M. S. Fee, D. W. Tank, and W. Denk, “A miniature head-mounted two-photon microscope: high-resolution brain imaging in freely moving animals,” *Neuron*, vol. 31, no. 6, pp. 903–912, 2001.
- [98] W. R. Zipfel, R. M. Williams, and W. W. Webb, “Nonlinear magic: multiphoton microscopy in the biosciences,” *Nat. Biotech.*, vol. 21, no. 11, pp. 1369–1377, 2003.

VITA

VITA

Dergan Lin received his B.S. degree in Electrical Engineering from Purdue University in 2009, and later received his M.S. degree in Electrical and Computer Engineering from Purdue University in 2012.